Investigation on influence of antimony tin oxide/silver nanofluid on direct absorption parabolic solar collector

Investigation on the influence of antimony tin oxide/silver nanofluid on direct absorption parabolic solar collector

Sreehari Sreekumar[a], Albin Joseph[b], Sujith Kumar C. S[a], Shijo Thomas[*b]

[a] Department of Mechanical Engineering, National Institute of Technology Calicut, 673601, India

[b]School of Materials Science and Engineering, National Institute of Technology Calicut, 673601, India

Corresponding author: Shijo Thomas, Email address: shijo@nitc.ac.in

Abstract

This paper discusses the synthesis and characterization of a novel hybrid nanofluid and its performance analysis on a parabolic trough direct absorption solar collector. Broadening the absorption spectra of working fluid using nanoparticles is the new research revolution for increasing the volumetric solar absorption efficiency. It is reported that plasmonic silver nanoparticles have higher absorption in visible spectra while antimony doped tin oxide has an absorption peak in the near-infrared region. Hence, antimony tin oxide/silver hybrid nanoparticle with broad spectral absorptivity was synthesized. Optimization of the nanofluid composition performed using response surface methodology yielded an optimized mass fraction of antimony tin oxide and surfactant, sodium dodecyl sulfate, as 0.1% each. The solar weighted absorption fraction of optimized nanofluid was obtained as 90.12%. Performance evaluation of the solar collector was based on ASHRAE standards 93-2010. The optical efficiency of the parabolic collector was calculated to be 75%. The maximum thermal efficiency obtained by the optimized nanofluid applied parabolic trough direct absorption solar collector was 63.5% at a flow rate of 0.022 kgs^{-1} and the highest exergy efficiency obtained was 5.6%. Thermal and exergy efficiency was observed to increase with increase in flow rate.

Keywords: ATO/Ag hybrid nanoparticle, solar weighted absorption fraction, optimization, direct absorption, photothermal conversion.

28 **Nomenclature**

English Parameters

A	Aperture area [m^2]	K	Geometric factor
C_p	Specific heat [$J\ kg^{-1}\ K^{-1}$]	L_a	Receiver tube length [m]
D_{out}	Outer diameter of the receiver [m]	$\dot{m}$	Mass flow rate [kgs^{-1}]
d	Universal non-random error parameter due to receiver mislocation and reflector profile errors	s_{in}	Entropy of heat transfer fluid at inlet [$kJkg^{-1}K^{-1}$]
		s_{out}	Entropy of heat transfer fluid at outlet [$kJkg^{-1}K^{-1}$]
		T_{amb}	Ambient temperature [K]
f	Focal distance [m]	T_{fm}	Mean fluid temperature [K]
h_{in}	Enthalpy of heat transfer fluid at inlet [kJ]	T_{in}	Inlet temperature of heat transfer fluid [K]
		T_{out}	Outlet temperature of heat transfer fluid [K]
h_{out}	Enthalpy of heat transfer fluid at outlet [kJ]	T_s	Temperature of the sun [K]
		Q_{sol}	Solar radiation intensity [W]
I	Solar intensity [Wm^{-2}]	W_a	Aperture width [m]
I_λ	Solar spectral intensity [$Wm^{-2}nm^{-1}$]		

Greek Parameters

α	Absorptance	λ	Wavelength [nm]
$\alpha_{receiver}$	Absorbance of reflector	τ	Transmittance
β	Universal non-random error parameter due to angular errors	τ_{cover}	Transmittance of the cover glass
		φ_r	Rim angle of collector [rad]
γ	Intercept factor	ψ	Exergy [W]
η_{ex}	Exergy efficiency	ψ_{dest}	Exergy destruction rate [W]
η_{th}	Thermal efficiency	ψ_{in}	Total exergy entering the system [W]
θ	Incidence angle [rad]	$\psi_{m,in}$	Exergy inflow rate by heat transfer fluid [W]
ρ	Reflectance	$\psi_{m,out}$	Exergy inflow rate by heat transfer fluid [W]
$\rho_{collector}$	Reflectance of collector sheet	ψ_{out}	Total exergy exiting the system [W]
σ	Universal random-error parameter	ψ_{sol}	Solar radiation exergy absorption rate [W]

Abbreviations

ASTM	American Society for Testing and Materials	NIR	Near-infrared
ANOVA	Analysis of Variance	PTDASC	Parabolic Trough Direct Absorption Solar Collector
DOE	Design of Experiments	RSM	Response Surface Methodology
LSPR	Localized Surface Plasmon Resonance		

1. Introduction

Cleaner and sustainable energy technologies are gaining importance due to the increase in environmental pollution and the current energy demand. Solar energy is a reliable and promising one among the renewable energy resources. Researches on increasing the energy conversion efficiency of solar energy systems are taking place at a burgeoning speed. Photothermal, photochemical and photovoltaic conversions are the prominent methods of solar energy utilization. Photothermal systems are having the highest energy conversion efficiency among the other solar energy conversion techniques. Among the solar thermal systems, concentrating solar collectors are having higher thermal efficiency compared to non-concentrating collectors. A typical concentrating solar collector is based on three main steps: (i) concentrating the solar radiation on the receiver surface, (ii) energy conversion at the absorber surface and, (iii) heat transfer from absorber surface to working fluid by convection and conduction [1]. In such systems, the maximum temperature is occurring at the absorber surface immersed in water due to which the heat loss to the surrounding increases. They also show an increase in thermal resistance during heat transfer from the absorber surface to the working fluid. Direct absorption Solar Collectors (DASC) works on the principle of volumetric absorption of solar radiation. Since water and thermal oils have poor optical absorption properties, nanofluids are used in DASC. The energy gain of fluid by convective heat transfer from surface absorbers in a conventional solar collector is transformed into radiative transfer in a participating medium (nanofluid) in DASC. Synthesizing nanofluids with a higher photo-thermal conversion rate improves solar absorption efficiency. Vast research on synthesis, characterization, and testing of nanofluids with high thermal conductivity and optical absorptivity, like Ag, Au, carbon nanotubes (CNT), Cu, graphite, graphene, and metal oxides, have been performed.

The concept of volumetric absorption was first proposed by Minardi et al. [2] in 1975. Tyagi et al. [3] were the first to propose a theoretical model for DASC. From the theoretical analysis, the direct absorption was found to have higher efficiency compared to surface absorption. Otanicar et al. [4] investigated the direct absorption capability of different base fluids by comparing their extinction coefficients and found water to better than thermal oils. Photothermal conversion of nanofluids synthesized using metal (Cu, Au, Ag), metal oxide (CuO, Al_2O_3, TiO_2) and nonmetal (GO, MWCNT) nanoparticles were performed over the years. Chen et al. [5] studied the photothermal conversion property of Au nanofluids and found that efficiency increased with an increase in the volume fraction of nanoparticle. Experimental analysis on the photothermal conversion property of gold nanofluids was performed by Beicker et al. [6]. Amjad et al. [7] analyzed the photothermal conversion capability of different nanofluids to be used for direct absorption applications. The results showed that silver nanofluid exhibited maximum energy conversion efficiency. Abdelrazika et al. [8] examined the influence of water-based silver nanofluid on the performance of hybrid photovoltaic-thermal collectors. Results showed that the transmittance of nanofluid decreased with an increase in collector depth and nanofluid volume fraction. Valizade et al. [9] performed an experimental investigation on direct absorption using nanofluids and metal foams of CuO and SiC material. Nanofluid absorber exhibited enhancement over its respective metal foam in the case of copper oxide. Chen et al. [10] performed photo-thermal conversion investigations on cupric oxide (CuO) and antimony tin oxide (ATO) binary nanofluid. ATO provided complementary optical absorption due to its better solar absorption at near-infrared (NIR) spectra. Investigation performed by Yu et al. [11] concluded that the dispersion stability of nanofluid is having a direct impact on optical absorptivity. Even though the property of base fluid could be enhanced by addition of nanoparticle, there are some limitations. Some of the drawbacks associated with nanofluids are the higher cost, time-consuming nanofluid synthesis process, lesser stability, and higher viscosity.

A hybrid nanoparticle has an advantage over mono-component nanoparticle as it exhibits synergetic properties of the multiple components present in the structure. Property tunability at particle level is the advantage of hybrid nanofluid over binary nanofluid. According to the authors' knowledge hybrid nanoparticles with selective spectral absorptivity are less explored. Yu et al. [12] synthesized CuO/Ag composite nanoparticle for solar direct absorption application. Jiang et al. [13] synthesized Ag-Ag_2S core-shell structure with broad absorption spectra which exhibited

an absorption peak in the wavelength range of 300 nm-1100 nm. Zeng et al. [14] synthesized $Sn/SiO_2/Ag$ core-shell PCM nanoparticle for thermal energy storage and solar absorption. Zeng et al. [15] synthesized silver-based SiO_2/Ag plasmonic hybrid nanofluid and its binary nanofluid with NIR absorbing MWCNT nanoparticle. Zeng et al. [16] synthesized a full spectrum absorption hybrid nanoparticle. Visible spectrum absorbing TiN nanoparticle and NIR absorbing magnetic Fe_3O_4 nanoparticle was selected as hybrid material components. This was one of the few papers on full spectral absorption hybrid nanoparticle.

Design of experiments (DoE), fuzzy logic and artificial neural network (ANN) are the most preferred tools for finding the interaction of input parameters on the output response. Out of these, DoE will provide an insight into the dependence of response on input parameters in a minimum number of experiments [17]. Esfe et al. [18] optimized the rheological and thermal properties of Al_2O_3-EG/water nanofluid by using response surface methodology (RSM).

The advantage of a DASC is that the maximum temperature is occurring within the fluid volume and hence the need for a hotter absorber tube surface can be avoided. In addition, the energy efficiency of the collector could be improved by increasing the solar spectral absorptivity of nanofluid by modifying the morphology, material property (thermal and optical) and mass fraction of the nanomaterial. The thermo-economic analysis was conducted on the performance of a DASC by Otanicar et al. [19]. The studies compared the economic and environmental impact of DASC on residential water heating applications and proved that in addition to 3% improvement in thermal efficiency of the collector, the DASCs are providing the same economic benefit as a conventional collector. Applicability of hybrid nanofluid in conventional parabolic trough collectors was extensively reviewed by Minea et al. [20]. However, experimental investigations performed on DASC using hybrid nanofluids are very rare compared to single and binary nanofluids. Bellos et al. [21] performed an investigation on the performance of a parabolic trough collector using oil-based Al_2O_3-TiO_2 hybrid nanofluid. The analysis shows that enhancement in the thermal efficiency of PTC using hybrid nanofluid was higher than the mono nanofluids. Delfani et al. [22] conducted experimental and numerical analysis on the thermal performance of MWCNT nanofluid based DASC for residential application and reported an improvement of 10-29% in thermal efficiency, over that of the base fluid. The efficiency was found to be an ascending function of volume fraction and flow rate. Vakili et al. [23] evaluated flat plate

DASC with graphene nanoplatelets as working fluid for domestic water heating applications. The maximum thermal efficiency was obtained at an optimum mass flow rate of 0.015 kgs^{-1}. Menbari et al. [24] on examining CuO as working fluid in PTDASC found that thermal efficiency of 52% was achievable by varying volume fraction of the nanofluid. Menbari et al. [25] performed an experimental analysis on CuO/Al_2O_3 binary nanofluid being applied in PTDASC. The thermal efficiency of PTDASC having binary nanofluid was found to be 48%. Although numerous works on energy analysis of DASCs has been reported, experimental works on the exergy analysis on direct absorption solar collectors are very few. An extensive review of the exergy analysis of solar collectors and its significance on the performance investigation was performed by Kalogirou et al. [26]. Gorji and Ranjbar [27] carried out thermal exergy analysis on DASC for optimizing the performance parameters of the system. Response surface methodology was used for optimizing the parameters like incident solar flux, nanofluid volume fraction and flow rate. Maryam Karami [28] reported an enhancement in the thermal efficiency of 21.7% for DASC with hybrid nanofluid over the base fluid.

From the literature review, it is clearly inferred that most of the hybrid nanoparticles synthesized have Ag as one of its components due to its LSPR effect. ATO is a viable option for nanoparticles with NIR absorption [10]. Among the available base fluids, water is reported to be having the highest optical absorptivity [4]. Investigations on hybrid nanofluids with wide spectrum solar absorption in PTDASC is also very limited in the reported literature. Design of Experiments (DoE) could be adopted as a useful tool for the optimization of parameters based on output response with a minimal number of experiments.

In this work, synthesis, characterization, and optimization of a novel ATO/Ag hybrid nanoparticle having broad spectral absorption property are performed. Based on the design of experiments concept a design matrix was created with different mass fractions of components based on which the synthesis and characterization of nanofluids were performed. Response surface methodology was adopted for finding the effect of nanoparticle and surfactant mass fractions on the solar weighted absorption fraction of nanofluid. The optimized mass fraction and surfactant concentration were calculated using the desirability function in 'Design Expert' software. Parametric study was also performed to analyze the effect of mass fraction of nanoparticle and the

143 penetration depth of light on optical absorptivity. Experimental investigations were conducted on
144 optimized hybrid nanofluid based PTDASC and, energy and exergy analysis were performed.

145 2. Synthesis and characterization of hybrid nanoparticle

146 *2.1. Synthesis of ATO/Ag hybrid nanoparticle*

147 ATO nanoparticle was supplied by Sigma Aldrich. The hybrid nanoparticle is synthesized using
148 facile one-step reduction reaction [15, 29] using Sb_2O_5, $SnCl_2$, HCl, $AgNO_3$ and ATO
149 nanoparticles (Sigma Aldrich). The ATO nanoparticles are dispersed in a medium of pH greater
150 than its isoelectric point (IEP). The IEP of tin oxide is in a range of +2 and +4 while the IEP of
151 Sb_2O_5 lies between +3 and +5 [30]. IEP of ATO lies in between the constituents. Hence the
152 particles will gain a negative charge on dispersion in base fluid [15]. 200 g of $SnCl_2$ and 300 µl of
153 HCl are mixed in 40 ml of DI water, and then ATO nanoparticles are dispersed in this medium.
154 The pH of the reaction environment is adjusted by rinsing in water continuously. pH is set to 7 for
155 further reaction process. ATO surface will have a negative charge in this reaction environment.
156 ATO nanoparticle is activated with Sn^{2+} by inorganic grafting between OH^- groups on the surface
157 [29]. $AgNO_3$ solution of 40ml is prepared and mixed with the above solution. ATO/Sn^{2+} wet
158 mixture on reaction with silver nitrate solution undergoes a reduction process to produce Ag+ ions
159 in solution. The charge difference is the potential for Ag deposition on the surface of ATO [29].
160 Finally, the deposited ATO/Ag nanoparticle is washed and dried in a hot air oven maintained at
161 60°C. The synthesis process is graphically represented in Fig.1.

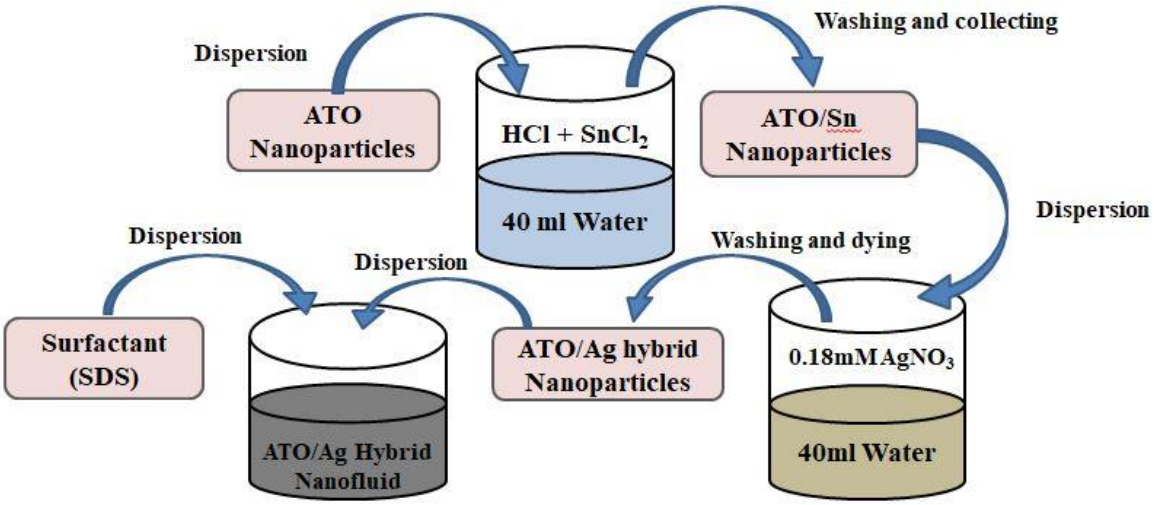

162

163 **Fig. 1.** Methodology used in the synthesis of ATO/Ag nanoparticle and nanofluid

2.2. Morphological characterization

Morphological characterization of nanoparticle was done using high-resolution transmission electron microscopy (Jeol/JEM 2100) and scanning electron microscopy (Zeiss HV ΣIGMA FESEM). Morphological analysis carried out using the SEM image given by Fig. 2 shows that the ATO nanoparticles are not fully spherical. The size of ATO/Ag nanoparticles is varying in the range of 20 – 50 nm. As observed in Fig. 2, it is obvious that the size of the Ag nanoparticle is less than 10 nm. The SEM image of ATO/Ag hybrid nanoparticles is seen to be in a clustered form due to its smaller size. The TEM image of hybrid nanoparticle as displayed in Fig. 3 confirms the deposition of Ag on the surface of ATO nanoparticle. SEM image is unable to show the crosslinking between the particles as the size of particles falls below 40nm and the shape of particles is not spherical. Hence the SEM-EDAX is performed to show the presence of silver particles in the as-prepared particle sample.

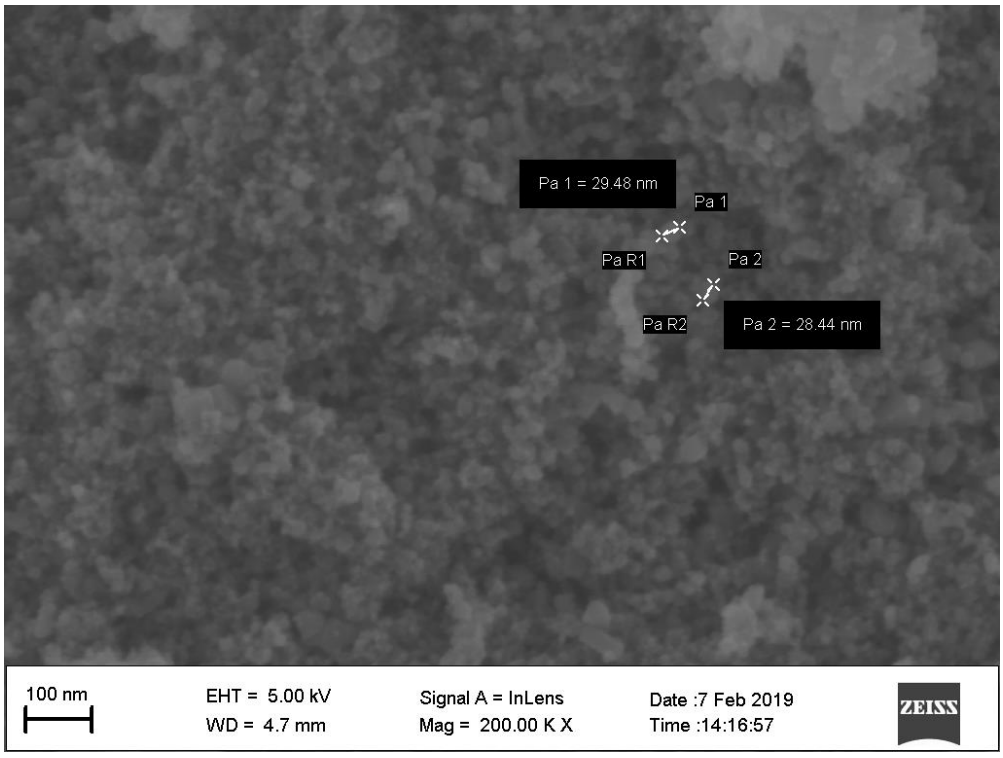

Fig. 2. SEM images of ATO/Ag hybrid nanoparticle

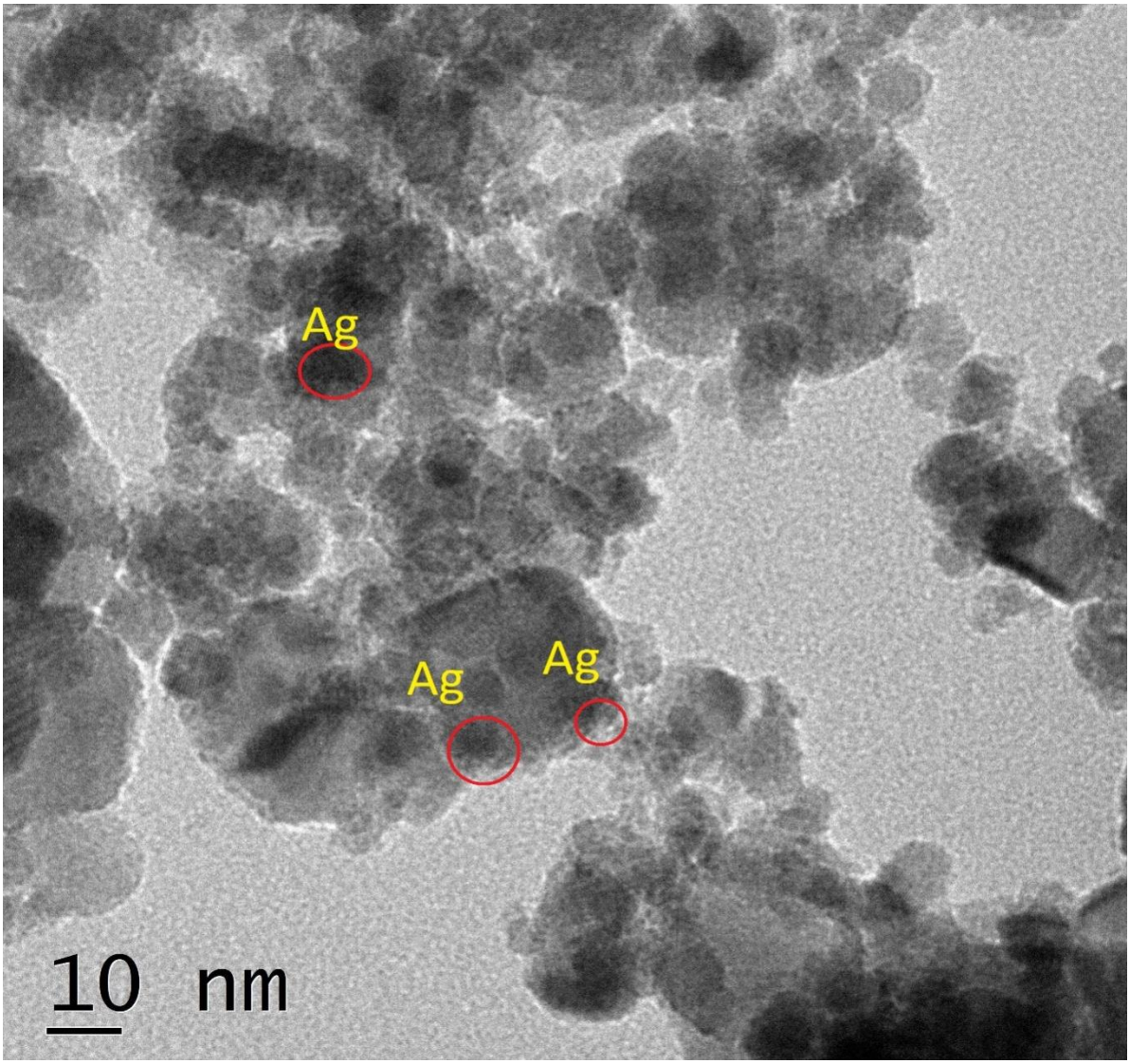

Fig. 3. TEM image of ATO/Ag hybrid nanoparticle

2.3. Phase structure analysis of hybrid nanoparticle

The XRD spectrum of ATO/Ag hybrid nanoparticle and ATO nanoparticles are shown in Fig 4. ATO nanoparticle is having tetragonal rutile structure. The major peaks of ATO nanoparticle corresponding to (100), (101), (200) and (211) crystallographic planes (JCPDS 88-0287) were observed in the XRD analysis. The peaks of Ag nanoparticle (JCPDS 04-0783) with FCC structure confirm the presence of Ag. FCC structured silver nanoparticle is having peaks that are indexed to its (111), (200), (220) and (311) crystallographic planes.

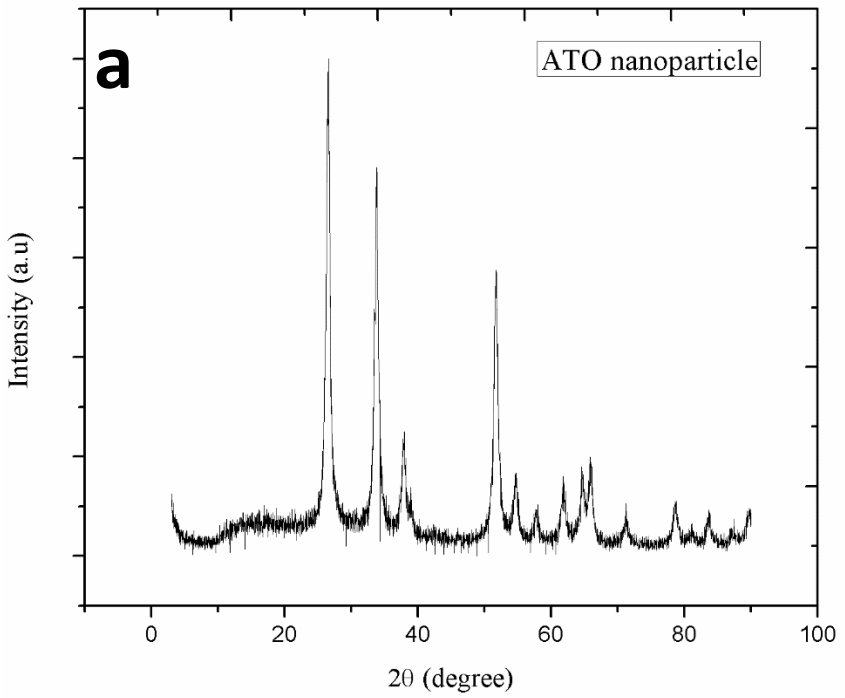

189

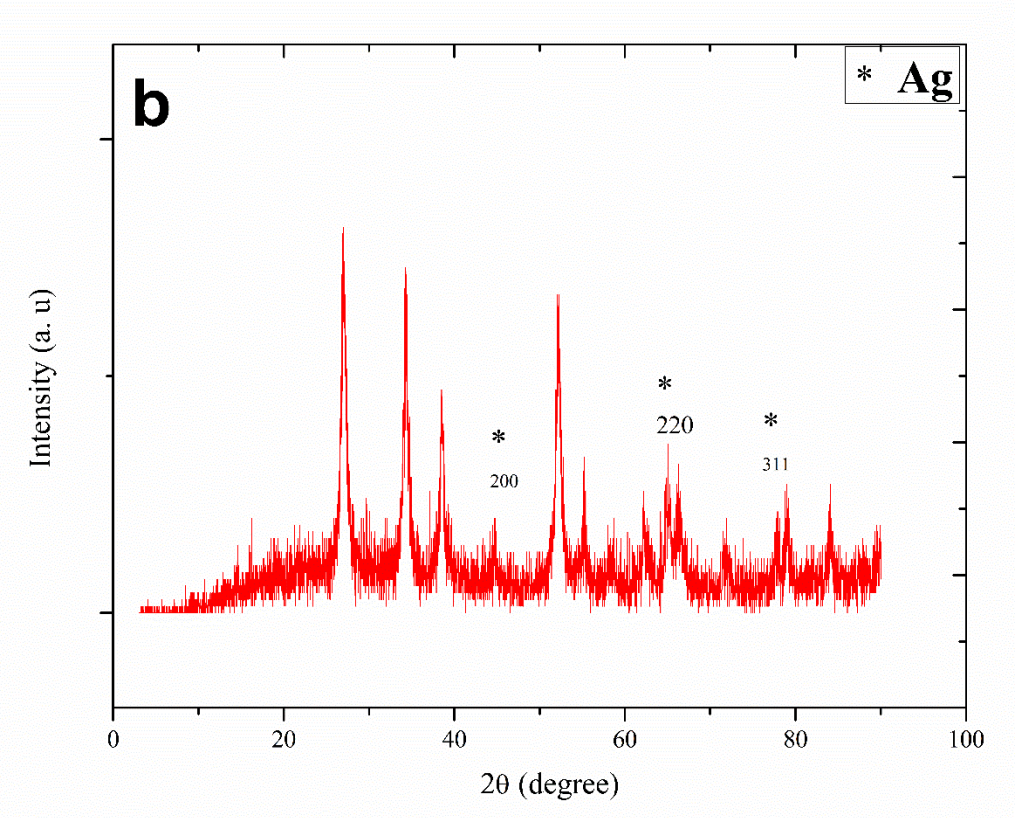

190

191 **Fig. 4.** XRD spectrum of (a) ATO nanoparticle, (b) ATO/Ag hybrid nanoparticle

2.4. Composition analysis of hybrid nanoparticle

Energy-Dispersive X-ray (EDAX) spectroscopic analysis is used to perform the elemental mapping of constituent elements present in a material. The composition of different elements of the synthesized hybrid nanomaterial was found by analyzing the X-rays emitted after bombarding with the electron beam from the test sample. Fig. 5 depicts the elemental distribution and composition in the ATO/Ag hybrid nanomaterial sample. The EDX spectroscopic results, as observed from Fig. 5, can also be used to confirm the presence of proposed elements in the hybrid material. The presence of ATO nanoparticle is confirmed by the occurrence of its main elements, Sn and Sb, which are having the maximum mass fractions of 66% and 10%. Ag which has 3% of mass fraction in the hybrid nanoparticle sample is also uniformly distributed in the sample, as observed from the mapping. As the size of the silver nanoparticle is almost half of ATO, the silver content in the area is less as observed from the mapping. From Fig. 5, it is inferred that the hybrid nanoparticles of the required components are synthesized, and have an even distribution of particles in the prepared sample.

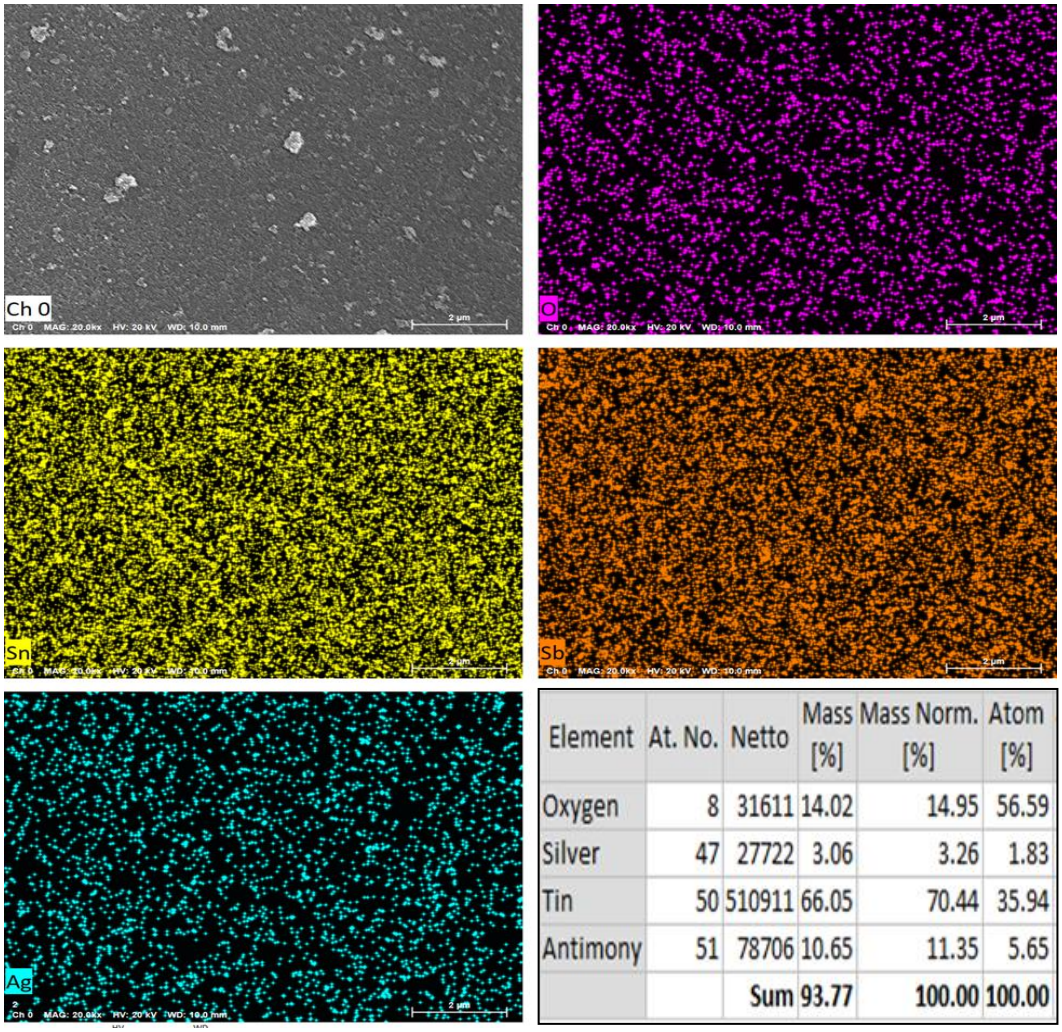

Element	At. No.	Netto	Mass [%]	Mass Norm. [%]	Atom [%]
Oxygen	8	31611	14.02	14.95	56.59
Silver	47	27722	3.06	3.26	1.83
Tin	50	510911	66.05	70.44	35.94
Antimony	51	78706	10.65	11.35	5.65
		Sum	**93.77**	**100.00**	**100.00**

Fig. 5: FESEM-EDAX mapping of ATO/Ag hybrid nanoparticle and composition table

3. Synthesis and characterization of Nanofluid

3.1. Preparation of nanofluid

The ATO/Ag hybrid nanoparticle is dispersed in DI water at the required mass fractions. For improving the stability of the prepared nanofluid, Sodium Dodecyl Sulfate (SDS) is added as surfactant. The addition of SDS as a surfactant produces surface charge on the particle which prevents the agglomeration of nanoparticles, thereby providing a highly stable and fully dispersed nanofluid. The surfactant-induced electrostatic dispersion stability is due to reduced inter-particle interaction [11].

Reducing the number of experiments to arrive at the optimum composition of ATO, Ag, and SDS is required to minimize the usage and waste of various chemicals. For obtaining the optimum composition that yields maximum optical absorption, response surface methodology (RSM) in Design Expert 10 was employed. RSM provides a clear insight of input variables interaction on output response using a minimum number of experimental runs [17]. The parameters considered for optimization are the concentrations of nanoparticle and surfactant. The mass fraction was varied from 0.01 to 0.2 % for ATO/Ag nanoparticle and 0.1 to 0.2% for SDS. The maximum limit of SDS concentration is selected so that the Critical Michelle Concentration (CMC) point is not reached. The maximum concentration of nanoparticles was selected based on the literature survey on the same individual nanoparticles. An increase in concentration was reported to increase the thermal conductivity but favors agglomeration. Hence the range that was reported in the literature to provide maximum absorption was taken as the limits of nanoparticles in the design matrix to find the optimum concentration. Stability analysis of the colloidal solution was performed for the mono-component ATO nanofluid, ATO/Ag hybrid nanofluid with optimized mass fraction and, ATO/Ag hybrid nanofluid with the maximum concentration of ATO/Ag from the design matrix as described in section 5.4.

According to the design matrix given in Table 1, different combinations of ATO, Ag, and SDS are subjected to spectroscopic analysis. Nine different combinations of constituent mass fractions and four same combinations of component mass fractions are presented in Table 1. A combination which is the mean of high and low levels is repeating four times in the design matrix. The reproducibility of the results is verified by cross-checking with the results obtained for repeated combinations. The response parameter based on which the optimized combination is arrived at is the solar weighted absorption fraction.

Table 1: Design matrix for preparing nanofluids with combinations of mass fraction

Run	Input Variables	
	ATO/Ag (% mass fraction)	SDS (% mass fraction)
1	0.01	0.15
2	0.11	0.15
3	0.11	0.1
4	0.11	0.15
5	0.11	0.15
6	0.04	0.11
7	0.17	0.19
8	0.11	0.2
9	0.04	0.19
10	0.17	0.11
11	0.2	0.15
12	0.11	0.15
13	0.11	0.15

3.2. Thermal conductivity

The thermal conductivity of the samples was measured with the KD2 Pro Thermal Property Meter (Decagon Devices). The KD2 Pro uses a transient line heat source method to obtain the transient temperature profile of fluid which is then compared with the full exponential integral solution of the heat equation to obtain the thermal conductivity. The measurements are done at a constant temperature of 29.5 °C for all samples. Three sets of readings were made for each sample and the average is taken as given in Table 2. The results reveal that the thermal conductivity of hybrid nanofluid samples is not a linear function of the concentration of nanoparticle and surfactant. Thermal conductivity values are given in Table 2.

3.3. Optical property characterization

UV-Vis spectrophotometer (SHIMADZU) with a spectral range of 280nm-1200nm is used for the optical characterization of the nanofluids. The wavelength range is sufficient in analyzing the optical absorptivity of broad-band spectral absorbing nanofluids as the complete extinction of radiation takes place in this spectral range [13, 31].

Table 2: Thermal conductivity and solar weighted absorption fraction of nanofluids

Run	Input Variables		Responses	
	ATO/Ag (% mass fraction)	SDS (% mass fraction)	Solar Weighted absorptivity (%) (Error range ±1.01%)	Thermal conductivity ($Wm^{-1}K^{-1}$) (Error range ±5%)
1	0.01	0.15	53.05	0.64
2	0.11	0.15	85.15	0.6654
3	0.11	0.1	91.63	0.65941
4	0.11	0.15	83	0.665
5	0.11	0.15	82.5	0.6656
6	0.04	0.11	74.03	0.64808
7	0.17	0.19	95.05	0.6665
8	0.11	0.2	82.6	0.65941
9	0.04	0.19	70.289	0.6491
10	0.17	0.11	93.54	0.667
11	0.2	0.15	98.9	0.67
12	0.11	0.15	84	0.6655
13	0.11	0.15	85.99	0.6654

The analysis is done in the wavelength corresponding to the solar spectrum ranging from visible to NIR range (280-1200μm). The optical path length of the beam is fixed as 10 mm. Beer-Lamberts

law given by Eq. (1) is used to find the extinction coefficient (K_e) of nanofluid from spectral transmittance coefficient ($\tau(\lambda)$), assuming that reflection and scattering are negligible.

$$\tau_\lambda = e^{-yK_e} = 1 - \alpha_\lambda \quad (1)$$

Transmittance spectra of nanofluids and the base fluid are shown in Fig. 6. The transmittance of nanofluid is compared with base fluid to indicate the decrease in transmittance ratio along the spectrum. Transmittance exhibited by nanofluid samples is showing a steep decrease at visible spectrum (350 nm – 450 nm) and NIR spectrum (950 nm – 1050 nm). This decrease in transmittance is due to the synergetic effect of ATO/Ag hybrid nanofluid having absorption peaks in the visible region (400 nm) and NIR region (1000 nm). Transmittance spectra can be considered to verify the presence of materials with absorption peaks in these above reported spectral range. From the transmittance spectra, radiative transmittance is observed to be a descending function of nanoparticle mass fraction. The highest transmittance is produced by the nanofluid with the least concentration (0.01% ATO/Ag). Least transmittance was provided by nanofluid with maximum nanoparticle mass fraction (0.2% ATO/Ag). For two samples, Run 6 (0.04% ATO/Ag 0.19% SDS) and Run 9 (0.04% ATO/Ag 0.11% SDS), with the same mass fraction of ATO/Ag, transmittance was found to be lower for the sample with lesser surfactant mass fraction. This trend of higher absorption at lower surfactant concentration is repeating for the two other samples, Run 7 (0.17% ATO/Ag, 0.19% SDS) and Run 10 (0.17% ATO/Ag, 0.11% SDS), with the same mass fraction. Noise observed in transmittance spectra above 1100 nm is due to the instrument.

The percentage of solar energy absorbed by the nanofluid volume is represented by the solar-weighted absorption fraction (Sm) calculated using Eq. (2) suggested by Drotning [32].

$$\mathrm{Sm} = \frac{\int_0^\lambda I_\lambda \alpha_\lambda d\lambda}{\int_0^\lambda I_\lambda d\lambda} \quad (2)$$

Fig. 7 depicts the spectral solar irradiance of nanofluid samples along with the reference spectrum. ASTM G-173 [32] at AM 1.5 standard is used as the reference spectra. Solar weighted absorptivity graph, when coinciding with reference spectra indicates a 100% radiation absorption by a nanofluid. The maximum solar absorption of 98.90% is displayed by Run 11 corresponding to the sample with the highest nanoparticle mass fraction (0.2%). The lowest spectral absorption is showed by the sample (Run 1) with the least concentration of nanoparticle (0.01%).

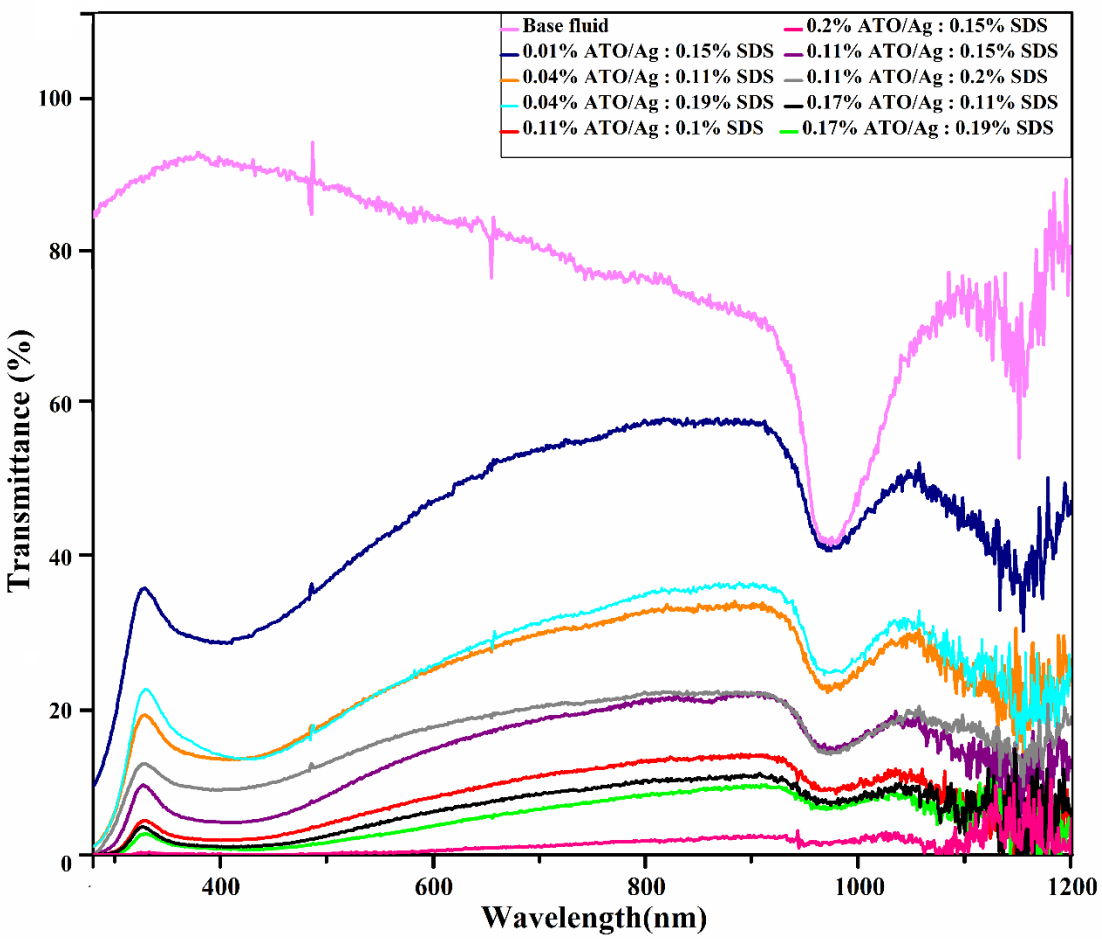

291

292 **Fig. 6.** Transmittance of nanofluid samples (Run 1, 2, 3, 6, 7, 8, 9, 10, 11) and water

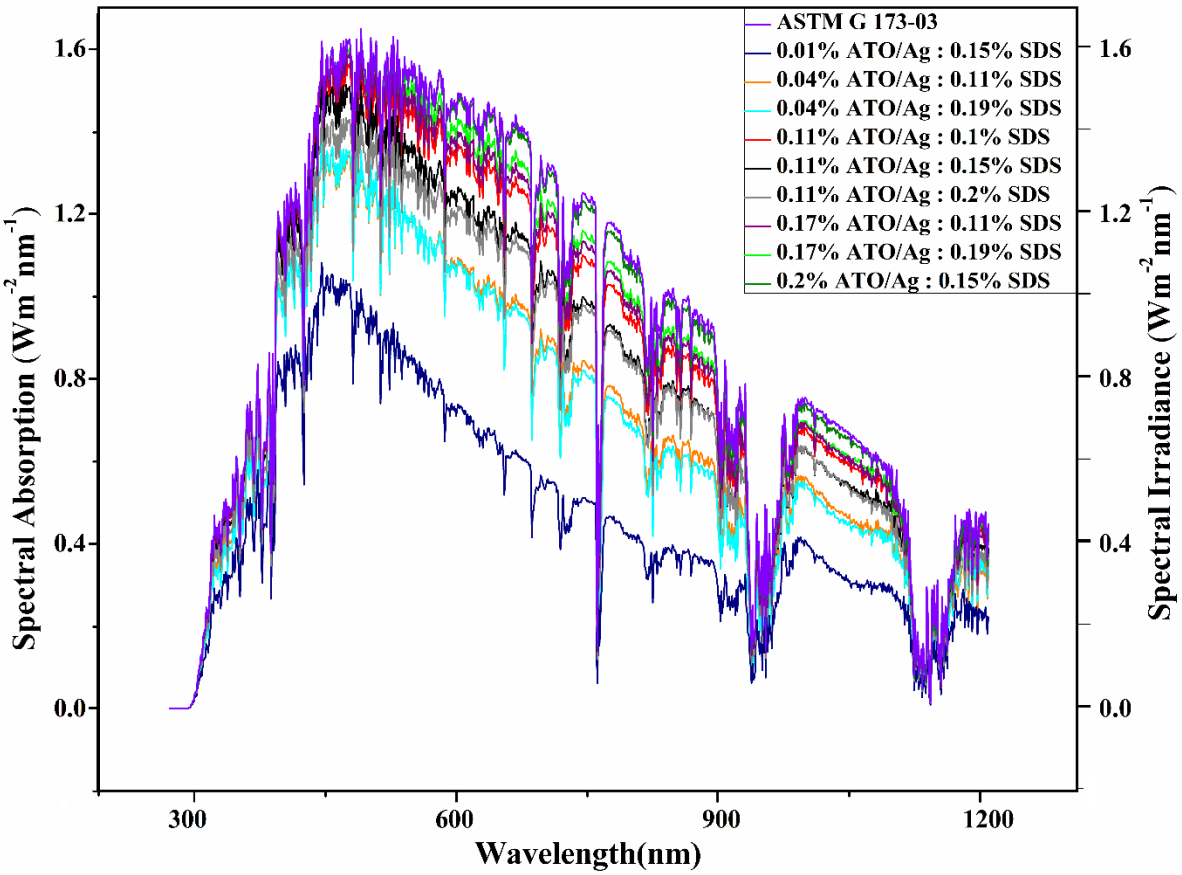

Fig. 7. Spectral irradiance of reference and nanofluid samples

4. Parametric study

4.1. Effect of penetration depth on solar weighted absorption fraction

The transmittance of nanofluid decreases with an increase in the penetration depth of radiation. Beer-Lambert law was used for studying the dependence of solar weighted absorption fraction on penetration depth. As observed in Fig. 8, the solar weighted absorption fraction is increasing exponentially with an increase in penetration distance. The influence of penetration depth on solar weighted absorption fraction is studied in a range of 0.2 - 10cm. Longer penetration distance provides improvement in solar weighted absorption fraction even though the concentration of nanofluid is less. Run 1 is having the lowest value of S_m at each penetration depth. From the variation of S_m plotted it is clearly observed that nanofluid with lesser concentration of

nanoparticles at shorter penetration depth is not preferred. A higher concentration of nanoparticle at longer penetration depth is also not advisable as the chances of agglomeration are prevalent.

Nanofluids with nanoparticle concentrations of 0.11% and above are having a solar weighted absorption percentage of 90 - 100% for penetration depth above 1.5 cm. Therefore, the dimension for nanofluid receiver volume must be above the optimum depth of penetration. The depth of penetration is not preferred to be increased much beyond the optimum depth as heat losses increase with an increase in surface area. Also, at higher optical path length, the complete radiation will be absorbed above a certain height and the resultant heat developed would have to be conducted to the remaining volume. Hence, it can be concluded that the optimum concentration at optimum penetration depth is required. In the present PTDASC system, since the inner diameter of the glass tube is 1.5 cm, it can be ensured that the extinction taking place in the fluid volume is greater than 95% for nanofluids with nanoparticle concentrations of 0.11% and above.

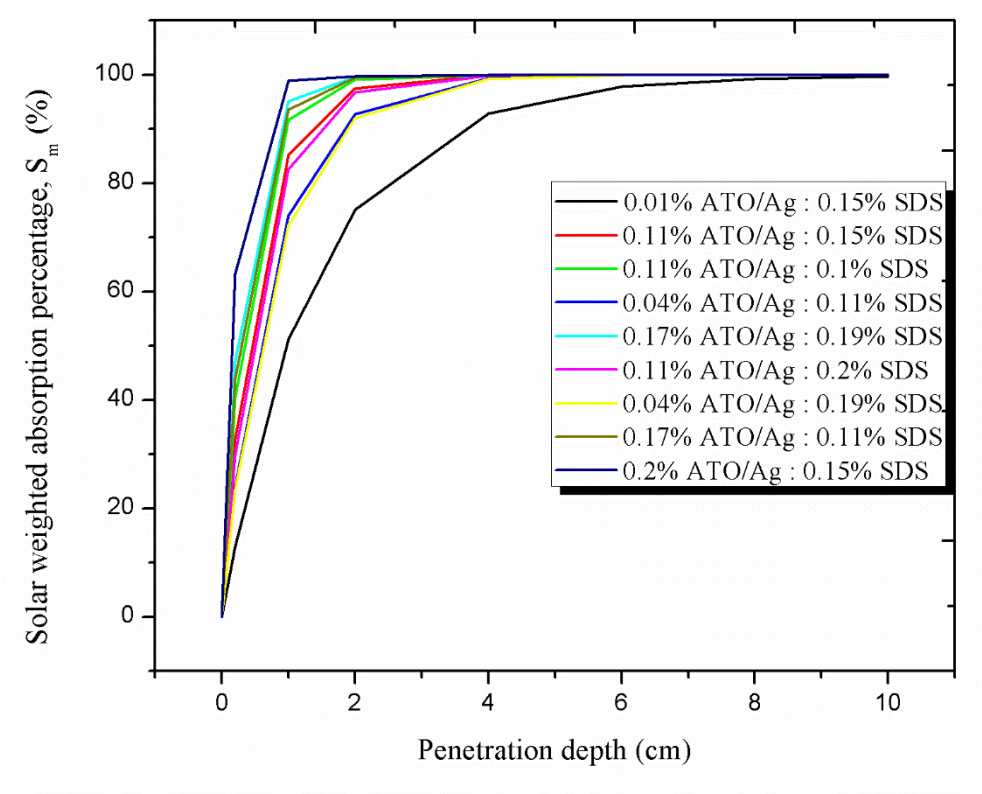

Fig. 8. Variation of solar weighted absorption percentage with penetration depth

4.2. Effect of mass fraction on the extinction coefficient

The effect of the mass fraction of nanoparticle on the extinction coefficient of nanofluid was investigated and plotted as given in Fig. 9. The investigations were performed on concentrations of nanoparticles corresponding to maximum (0.2%), average (0.11%) and minimum (0.01%), at wavelengths ranging from 300 nm to 900 nm. As observed in Fig. 9, the extinction coefficient is observed to be approximately a linear function of the mass fraction. Hence, absorption efficiency is increasing with optical path length for a specified concentration and, with increasing concentration for a specified light path length. Surmising from the parametric analysis, the solar radiation can be absorbed by either increasing the concentration or optical depth of penetration. By controlling the mass fraction of nanoparticle, the solar radiation can be absorbed completely for a specific optical depth. An error bar is also provided with the extinction curve to show the deviation involved in the measurement of values.

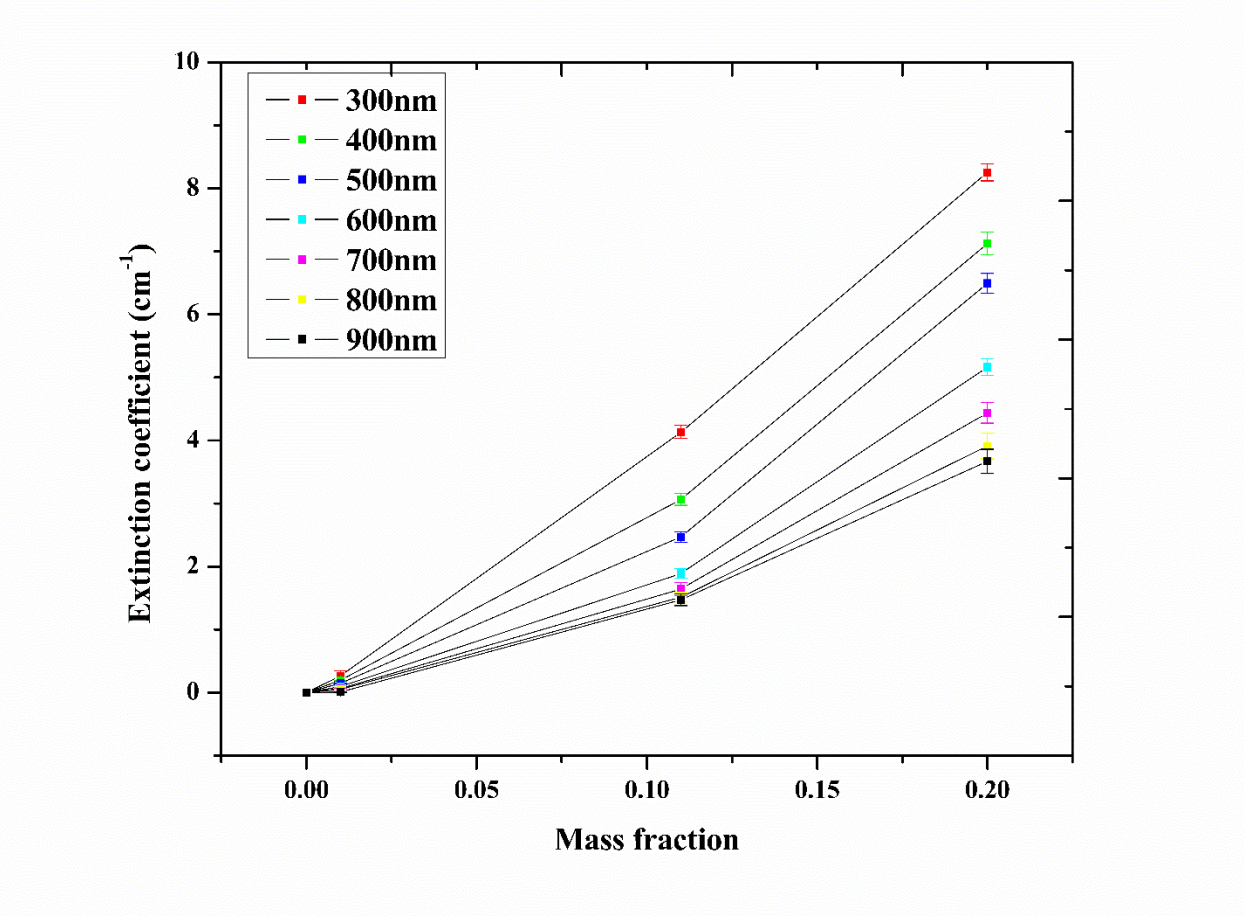

Fig. 9. Variation of extinction coefficient with mass fractions of nanoparticle

5. Optimization of mass fraction using Response surface methodology

5.1. ANOVA analysis of Solar Weighted Absorption Fraction

Analysis of variance (ANOVA) of the solar weighted absorption fraction is presented in Table 3, which provides information on the significant parameters in the designed model. The model is significant as the p-value is less than 0.0001. A, B, $A^{2,}$ and AB^2 are the significant model terms as their p-value is less than 0.1. ATO/Ag nanoparticle concentration is the most significant independent parameter among the factors since it is having the highest F value. The lack of fit being insignificant indicates that the model obtained is a correct fit. The difference between predicted R-squared and adjusted R-squared being less than 0.2, as shown in Table 6, implies the terms are in agreement. Furthermore, the value of R-squared and adjusted R-squared which are 0.9839 and 0.9678 respectively, implies the model is fitting perfectly. Adequate-precision, which measures the signal to noise ratio, is greater than the desired value of 4. The coefficient of determination (R-squared) value obtained was found to be greater than the good-fitting criterion of 0.8. Finally, the standard deviation of 2.16 points out the accuracy of the experiments.

Table 3: ANOVA of solar weighted absorption fraction

Source	Sum of Squares	Df	Mean Square	F Value	p-value Prob > F	Significance
Model	1709.55	6	284.93	61.07	< 0.0001	Significant
A-ATO/Ag	1051.11	1	1051.11	225.28	< 0.0001	
B-Surfactant	28.13	1	28.13	6.03	0.0494	
AB	6.89	1	6.89	1.48	0.2698	
A^2	92.98	1	92.98	19.93	0.0043	
B^2	25.49	1	25.49	5.46	0.0581	
AB^2	52.89	1	52.89	11.34	0.0151	
Residual	28.00	6	4.67			
Lack of Fit	19.54	2	9.77	4.63	0.0911	not significant
Pure Error	8.45	4	2.11			
Cor Total	1737.55	12				

Std. Dev.	2.16	R^2	0.9839
Mean	83.06	Adjusted R^2	0.9678
C.V. %	2.60	Predicted R^2	0.8161
PRESS	319.55	Adequate Precision	28.926

An empirical correlation for solar weighted absorption fraction which was obtained from the model developed for predicting responses for each level of factors, is given by Eq. (3). The significance of the various factors cannot be inferred from coefficients in the equation as they are scaled to the appropriate unit. As observed from Fig. 10, the values of solar weighted absorption fraction obtained from experimental data and model predicted values are in good agreement. The error was observed to be falling within ±2%.

$$\text{Solar Weighted Absorption Fraction} = +245.66320 - 1049.46831 * ATO/Ag - 2499.66608 * Surfactant + 18926.22192 * ATO/Ag * Surfactant - 810.18006 * (ATO/Ag)^2 + 7961.96978 * (Surfactant)^2 - 61244.95027 * ATO/Ag * (Surfactant)^2 \quad (3)$$

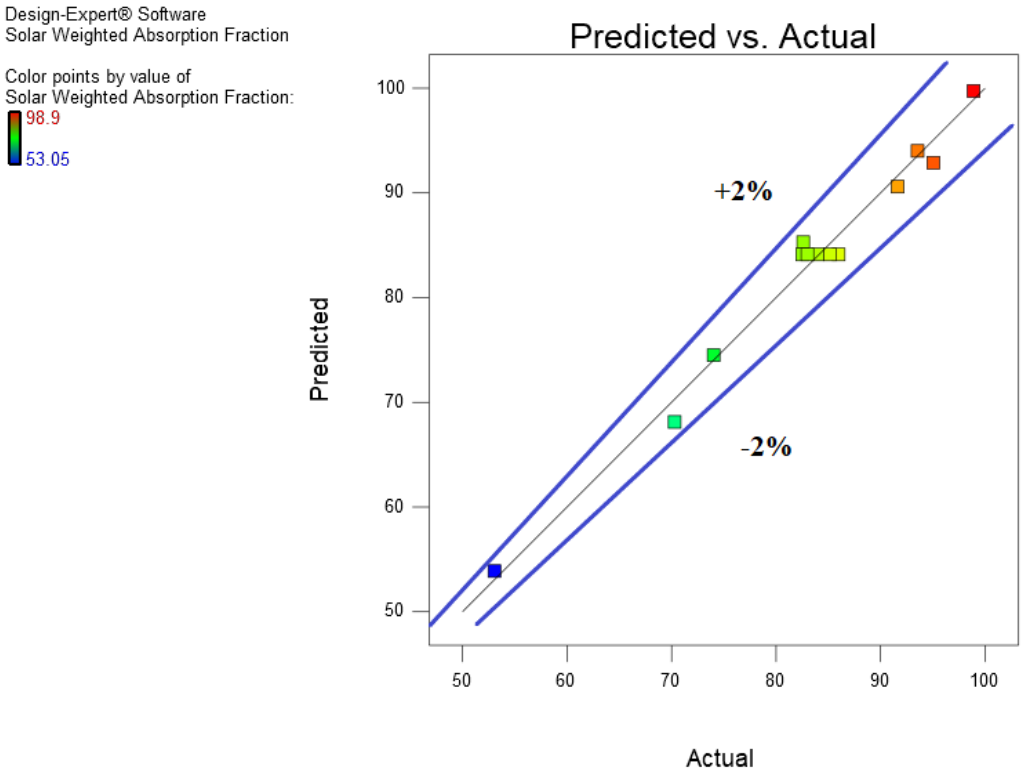

Fig. 10. Comparison between predicted values and actual values of S_m

356 *5.2. Interaction effect of process parameters on Solar weighted absorption fraction*

357 The 3D plot of absorption fraction with respect to ATO/Ag and SDS mass fraction, given by Fig.
358 11, clearly specifies that even though absorptivity increases with an increase in nanoparticle
359 concentration, the extreme surfactant concentration is seen to influence the absorption fraction. At
360 minimum nanoparticle concentration, the absorption fraction is observed to be higher at the highest
361 and the lowest surfactant concentration. The absorption fraction tends to increase with ATO/Ag
362 nanoparticle concentration and then decreases at maximum nanoparticle concentration, for both
363 high and low surfactant concentrations.

364

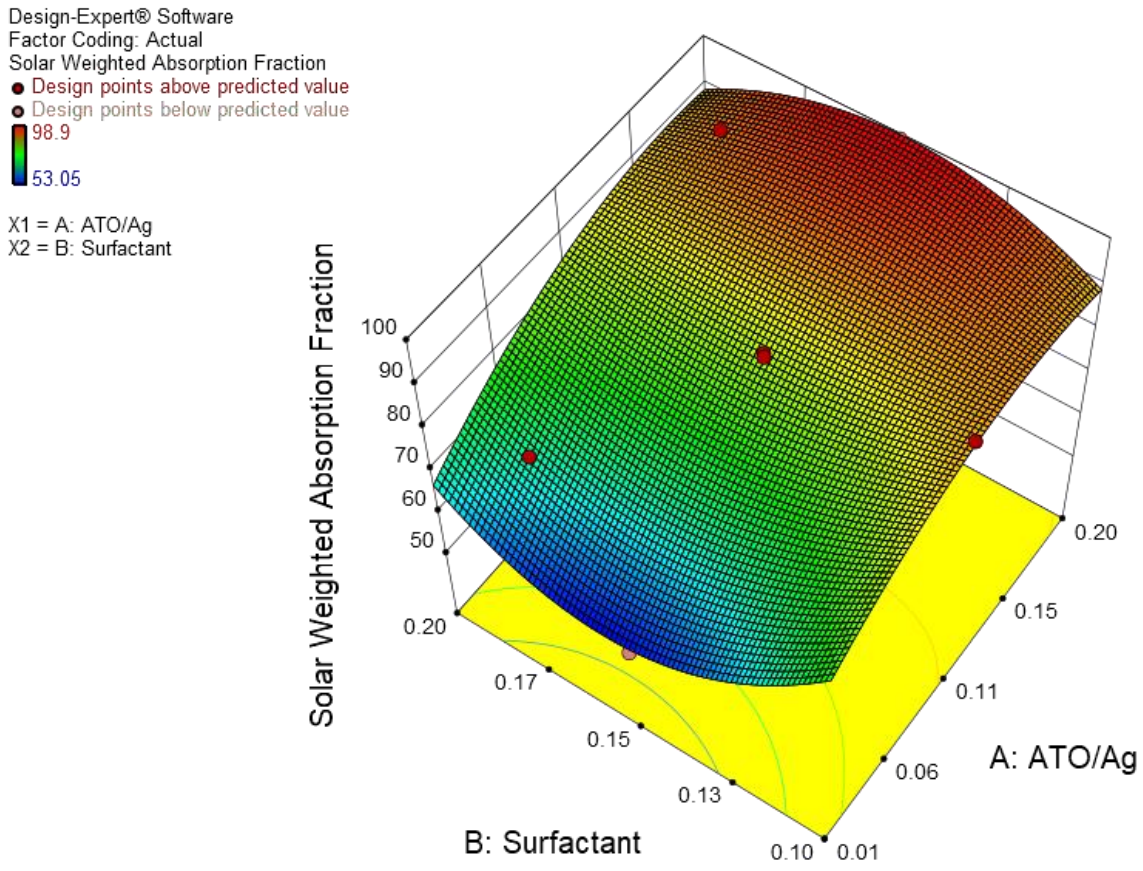

365

366 **Fig. 11.** Interaction effect of ATO/Ag and surfactant mass fractions on S_m: 3D surface.

367 As seen from the 2D plot of factors given by Fig. 12, ATO/Ag mass fraction is having the most
368 influence on solar weighted absorption fraction. The maximum absorption fraction of 98.9%

occurs at the highest concentration of nanofluid. For the samples Run 7 (0.17% ATO/Ag - 0.19% SDS) and Run 10 (0.17% ATO/Ag - 0.11% SDS), having the same nanoparticle mass fractions, the solar weighted absorption fraction was calculated to be 95% and 93.5% respectively. Hence the effect of surfactant concentration on solar weighted absorption is minimal.

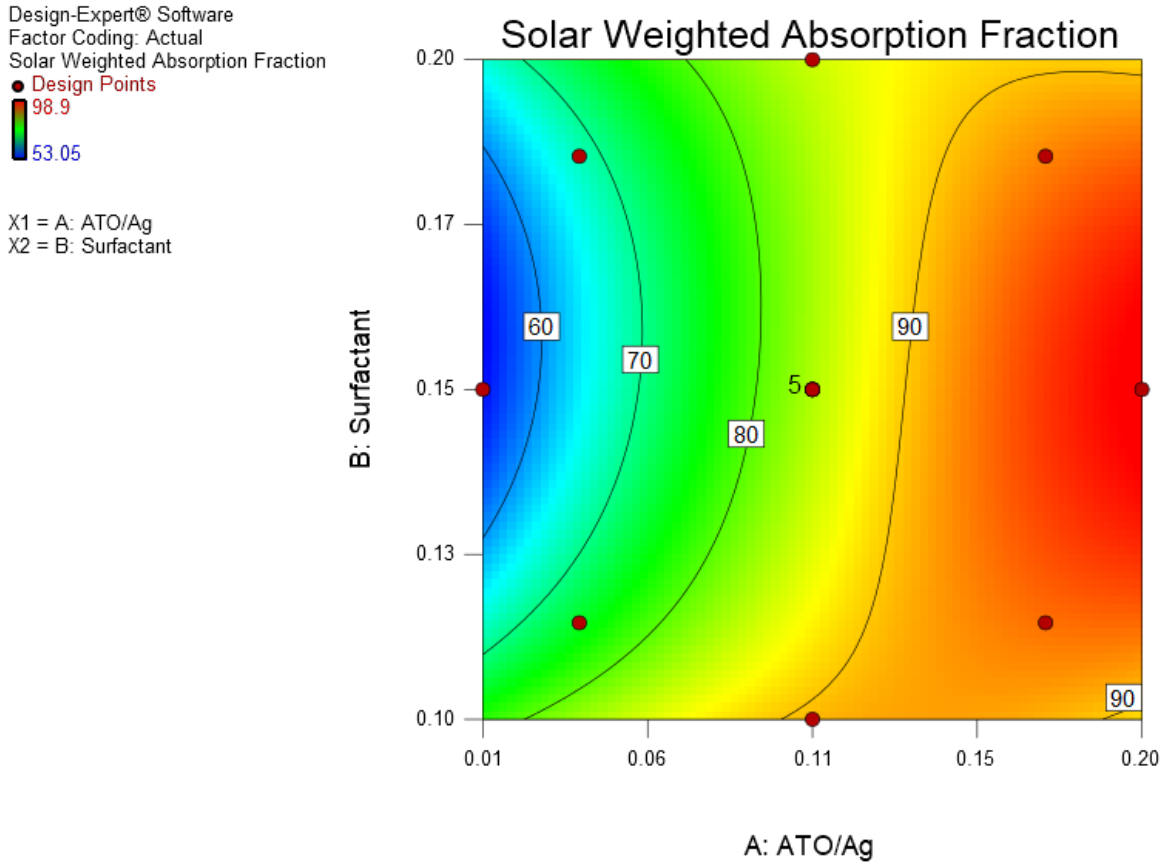

Fig. 12. Interaction effect of ATO/Ag and surfactant mass fractions on S_m: contour plot.

As discussed in Section 3.2, since the enhancement in thermal conductivity by the addition of nanoparticles was falling in the uncertainty range of the instrument, the optimization was performed based on a single response variable i.e. solar weighted absorption fraction.

5.3. Optimization of variables using desirability function

The DOE model was created for statistically optimizing the response variables to obtain an optimum value of inputs. From the model developed, solar weighted absorption fraction at each

factor levels are also obtained. Desirability is the objective function used for optimization. The weightage for variables can be adjusted on a scale of 1 to 5 [27, 34 and 35]. Increasing the weightage drives the output response towards the desired goal. Weightage of 3 was provided for solar weighted absorption fraction [35]. Desirability ranges from a minimum of zero to a maximum one. The maximum desirability provided by an operating condition is found by numerical optimization and was obtained as 0.532. The optimized concentrations of both ATO/Ag and SDS were obtained as 0.10%. The solar weighted absorption fraction predicted for the optimized condition is 90.12%. The weighted absorption fraction for the obtained optimum mass fraction was calculated experimentally and found to be 89% which is having a negligible error of 1.2% with the predicted value.

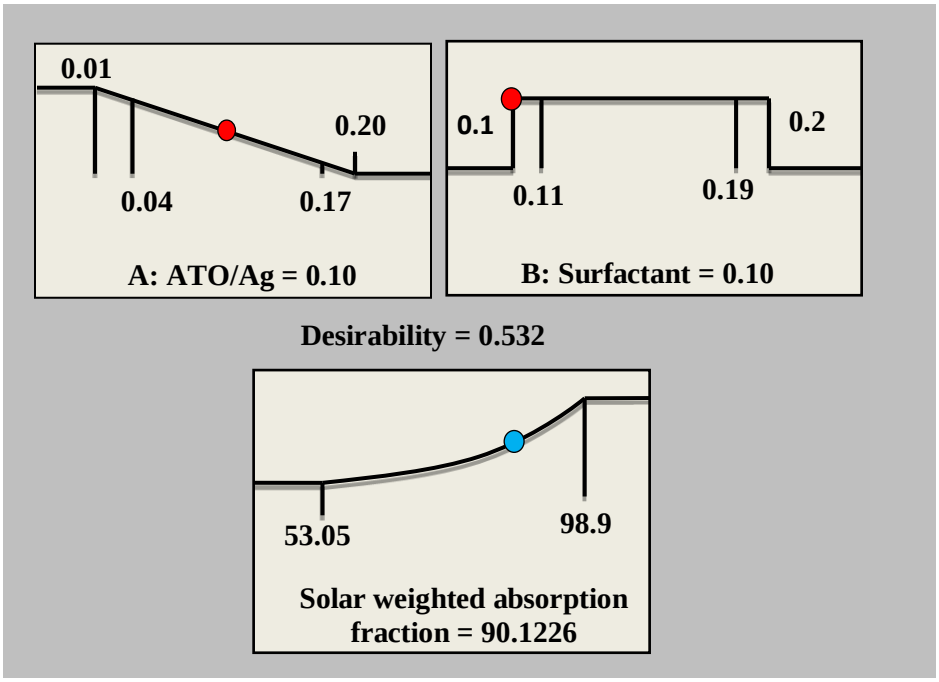

Fig. 13. Ramp function graph of desirability for numerical optimization

5.4. Stability analysis of optimized nanofluid

The sedimentation method was employed for investigating the stability of nanofluid [36] as shown in Fig. 14. On visual inspection, the ATO/Ag hybrid nanofluid was found to possess better stability compared to ATO nanofluid. The settling of ATO nanoparticles was prominent after 7 days from the synthesis date. Complete segregation of ATO nanoparticles was observed within 30 days after the synthesis. The optimized nanofluid (0.1% ATO/Ag) and nanofluid sample with maximum

concentration (0.2% ATO/Ag) exhibited better stability for 30 days with negligible segregation. The optimized concentration was found to have achieved better dispersion stability compared to nanofluid with 0.2% mass fraction for a longer time duration of 150 days.

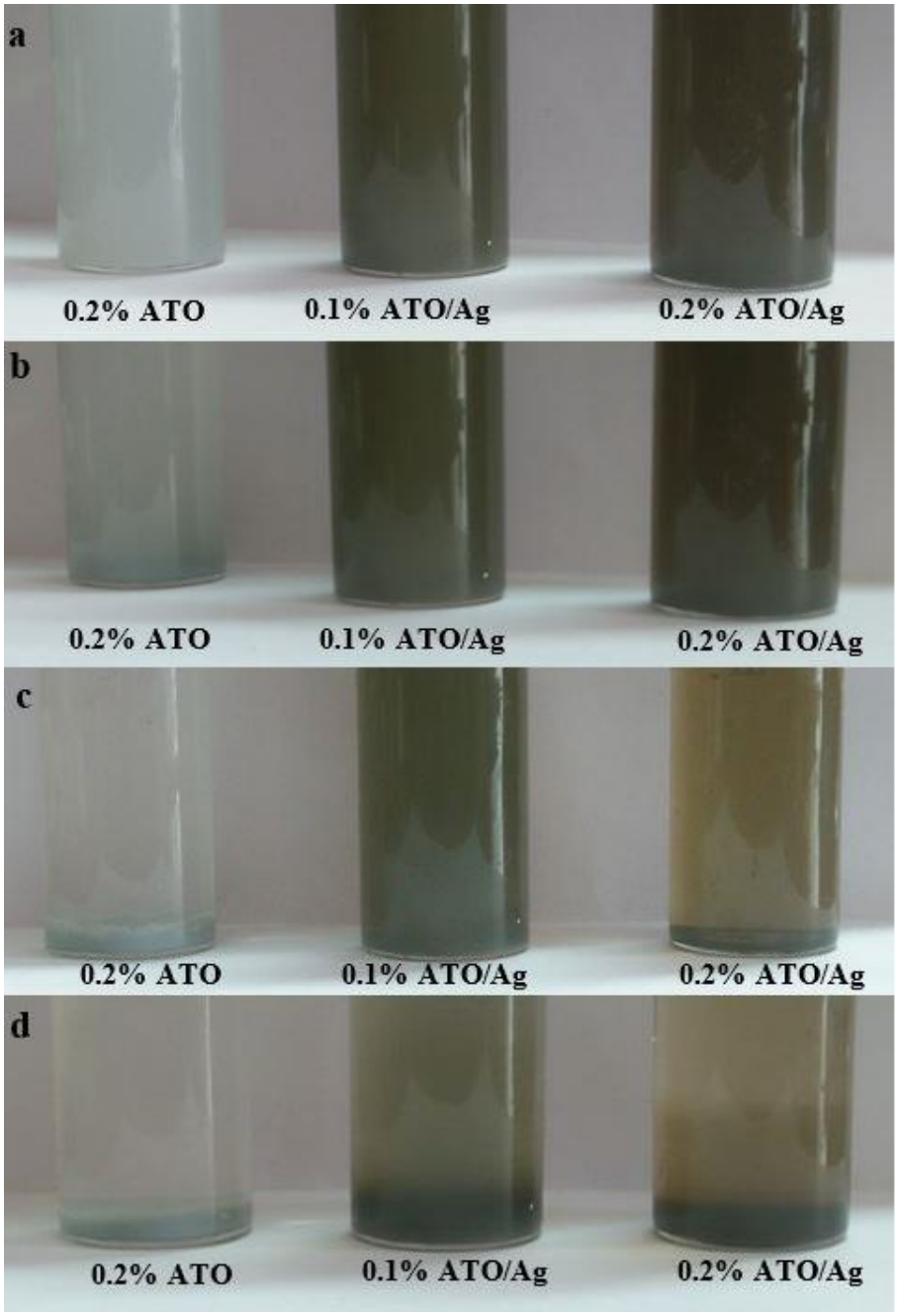

Fig. 14. Visual inspection on the stability of nanofluid after synthesis for a period of (a) 30 minutes (b) 7 days (c) 30 days (d) 150 days

6. Experimentation on Parabolic trough direct absorption solar collector

6.1. Reflector and absorber tube

The solar thermal collector system consists of a parabolic shaped reflector mirror, a glass cover and a receiver tube placed at the focal point of the reflector. The focal point is at a distance of 0.27 m from the vertex. The parabola and receiver dimensions are given in Table 5. The receiver tube is a quartz tube with high optical transmittance. A glass cover was used for preventing the convective heat loss from the receiver tube surface to the environment. The annular space is filled with air and sealed at both ends to prevent the effect of wind. The working fluid is flowing inside the receiver tube. Volumetric absorption of the concentrated solar rays occurs inside the fluid volume in the receiver tube. The shape and focal point of parabolic reflectors are given by Eq. (4) and Eq. (5) respectively.

$$y = 0.925x^2 \tag{4}$$

$$f = \frac{W_a}{2} cot\varphi_r + \frac{{W_a}^2}{16f} \tag{5}$$

F Focal distance (m)

W Aperture width (m)

φ Rim angle (degree)

Table 5: Dimensions of the receiver tube

Parameters	Dimensions
Absorber tube inner diameter	15 mm
Absorber tube outer diameter	18 mm
Glass cover inner diameter	36 mm
Glass cover outer diameter	40 mm
Length of the receiver tube	1500 mm
Aperture width	1080 mm
Focal point	270 mm

6.2. *Hydraulic cycle*

The hydraulic cycle of the collector system was based on ASHRAE Standard 93-2010 as shown in Fig. 15. The fluid flow is controlled using the main valve and a bypass valve. The bypass valve was installed for the low flow rates according to the ASHRAE standards. The concentrated solar radiation is absorbed by the nanofluid while passing through the receiver tube. The temperatures at the inlet and exit were measured using calibrated T-type thermocouples with an accuracy of 0.5 $^{\circ}$C. Rotameter present at the flow outlet will measure the fluid flow rate through the cycle. The absorbing fluid enters the heat exchanger to reject heat and is pumped back through the cycle.

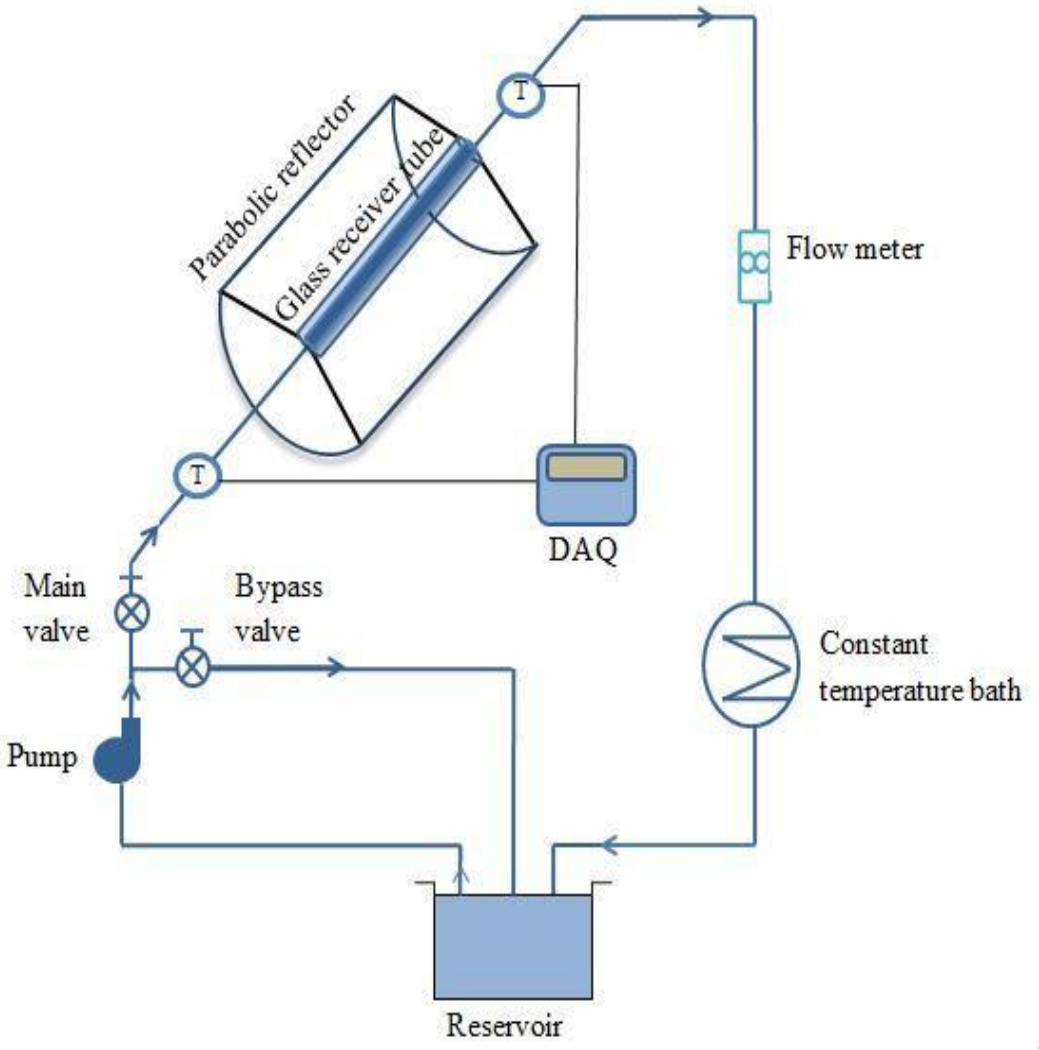

Fig. 15. The schematic of the hydraulic cycle

The actual experimental setup is shown in Fig. 16. A single-axis solar tracking was performed for the experiment. The automated solar tracker aligns the position of the reflector directly towards the radiation. The incidence angle is having a predominant effect on the thermal efficiency of the collector [37]. Hence, after experimenting on a range of incidence angles between 0° and 20°, the inclination equal to the incidence angle (11.3°) was found to be providing higher efficiency. Providing an inclination equal to the incidence angle, will decrease the shadowing at the ends and allows direct solar irradiation. The solar intensity was measured using an industrial standard pyranometer with an accuracy of $\pm 5 W^{-2}$.

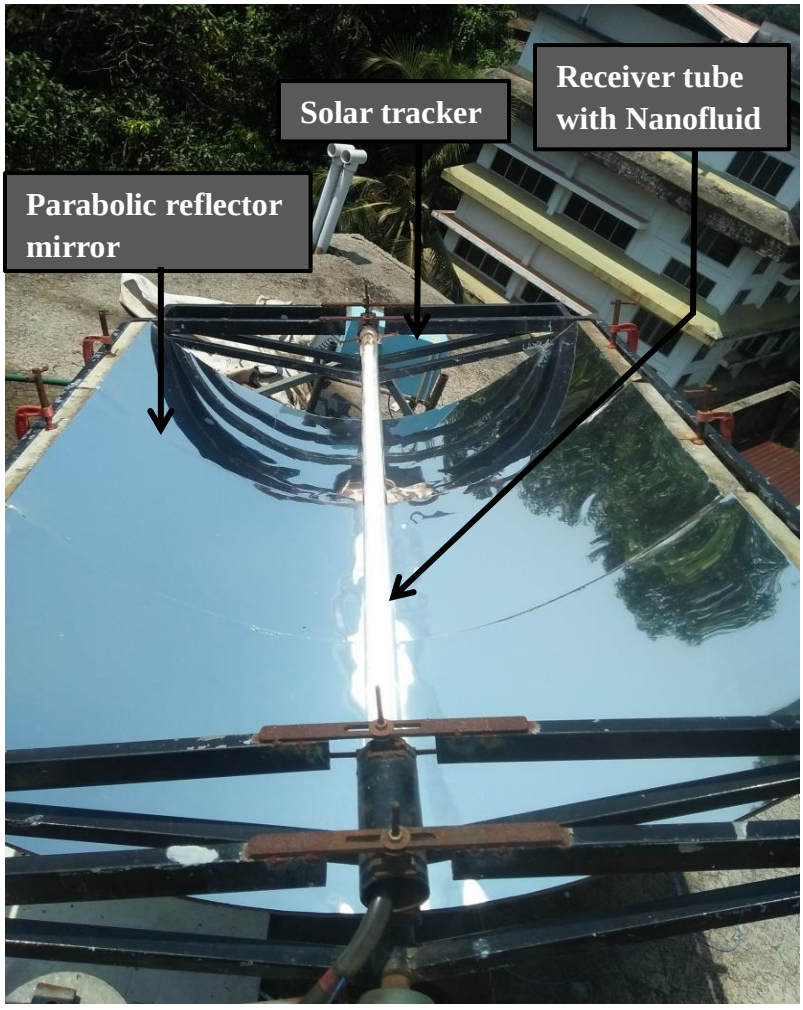

Fig. 16. Experimental setup of PTDASC

6.3. Performance evaluation methodology of PTDASC

6.3.1. Thermal efficiency

Instantaneous thermal efficiency was calculated at a time step of 5 minutes during the test day. Thermal efficiency calculated using Eq. (6), is the ratio between useful thermal energy of nanofluid to the total energy received by the parabolic trough collector.

$$\eta_{th} = \frac{\dot{m} C_{p,h} \Delta T}{IA} \tag{6}$$

6.3.2. Optical efficiency

The optical efficiency of the collector is obtained by considering all the optical materials that are occurring in the path of the light beam. Geometric and intercept factors need to be found out for calculating the optical efficiency using Eq. (7) [38]. Geometric factor, K, given by Eq. (8), is a measure of the effective reduction of the aperture area due to abnormal incidence effects. The intercept factor, γ, is the ratio of the energy intercepted by the receiver to the energy reflected by the reflector. A MATLAB code was generated to solve Eq. (9) using Simpson's one-third rule, to find the intercept factor. Geometric factor, intercept factors, and solar collector material properties were used to find the optical efficiency at each incidence angle using Eq. (7). The Intercept factor [39] was found to be 0.9228 from Eq. (9).

$$\eta_{optical} = (\rho_{collector} \tau_{cover} \alpha_{\ receiver}) * \gamma * \left(1 - A_f tan\,\theta\right) cos\theta \tag{7}$$

$$K = 1 - \left(\frac{D_{out}}{L_a} + \frac{f}{L_a} \left(1 + \frac{W_a^2}{48 {L_a}^2} \right) \right) tan\theta \tag{8}$$

$$\gamma = \frac{1+cos\varphi_r}{2sin\varphi_r} \int_0^{\theta_r} erf\left(\frac{sin\varphi_r (1+cos\theta)(1-2_d sin\theta) - (\pi_\beta (1+cos\varphi_r))}{\sqrt{2}\pi_\sigma (1+cos\varphi_r)} \right) + - erf\left(- \frac{sin\varphi_r (1+cos\theta)(1+2_d sin\theta) + (\pi_\beta (1+cos\varphi_r))}{\sqrt{2}\pi_\sigma (1+cos\varphi_r)} \right) \frac{d\theta}{1+cos\theta} \tag{9}$$

6.3.3. *Exergy efficiency*

Exergy is defined as the maximum useful work that can be extracted from a system at a given state in a specific environment. Exergy analysis is crucial in analyzing the potential of solar thermal systems.

Assumptions for exergy analysis:

1. Kinetic and potential energies are neglected
2. Chemical and nuclear interactions are neglected
3. Energy flow into the system and the work done by the system is taken as positive.
4. Exergy due to pressure drop is neglected.

Based on the assumptions stated above, an exergy balance across the receiver was formulated as shown in the Eq. (10-15). The exergy efficiency of the PTDASC is given by Eq. (15). Exergy from solar radiation and fluid flow are the significant contributing factors in the exergy balance of the concerned PTDASC.

$$\Sigma\psi_{in} - \Sigma\psi_{out} = \psi_{dest} \tag{10}$$

$$\psi_{sol} + \psi_{m,in} - \psi_{m,out} = \psi_{dest} \tag{11}$$

Where the $\psi_{m,in}$ and $\psi_{m,out}$ are calculated by using Eq. 12 and Eq. 13 respectively.

$$\psi_{m,in} = (h_{in} - h_{amb}) - T_{amb}(s_{in} - S_{amb}) \tag{12}$$

$$\psi_{m,out} = (h_{out} - h_{amb}) - T_{amb}(s_{out} - S_{amb}) \tag{13}$$

Incident solar power received by the parabolic collector is obtained by multiplying the collector aperture area with instantaneous solar radiation intensity as given by Eq. (14).

$$Q_{sol} = IA \tag{14}$$

Parabolic trough utilizes only beam radiation which can be assumed to be undiluted. Petela's exergy efficiency model [40] was used for finding the maximum power available from the incident solar radiation. The Sun was taken as the radiation reservoir which is having a temperature of 5770K. The maximum work potential from solar radiation is calculated by multiplying the solar exergy efficiency with incident solar power, as shown in Eq. (15).

$$\psi_{sol} = \left(1 - \frac{4T_{amb}}{3T_s} + \frac{1}{3}\left(\frac{T_{amb}}{T_s}\right)^4\right) * IA \tag{15}$$

The Eq. (16), as described below, is obtained by substituting Eqs. (12), (13) and (15) in Eq. (11).

$$\psi_{dest} = \psi_{sol} - \dot{m}C_p\left((T_{out} - T_{in}) - T_{amb}ln\left(\frac{T_{out}}{T_{in}}\right)\right) + \frac{mT_{amb}\Delta P}{\rho T_{fm}} \tag{16}$$

The irreversibility term due to pressure drop in Eq. (16) can be ignored as the effect is less significant [41]. The higher density of liquid working fluids, compared to gaseous ones, account for the fact that irreversibility due to pressure drop in parabolic trough collector can be neglected while using liquid working fluids [42]. The exergy efficiency of the system is calculated using Eqn. (17).

$$\eta_{ex} = 1 - \left(\frac{\psi_{dest}}{\psi_{sol}}\right) \tag{17}$$

6.3.4. Uncertainty analysis

The uncertainty analysis was performed for quantifying the accuracy of the measurements. Error analysis was conducted to find the errors associated with the thermal efficiency and exergy efficiency. Uncertainties for thermal efficiency and exergy efficiency were calculated using the Moffat method [43] as described in Eq. 18 and Eq. 19 respectively. The uncertainty associated with measurement of temperature, incident solar radiation, and the flow rate is ± 1.4%, ± 0.625% and ± 2.5%, respectively. The precision error occurring during the measurement of the extinction coefficient was taken into consideration and overall uncertainty in the measurement of the extinction coefficient was calculated to be ±0.8 %. The mean uncertainty involved in the

calculation of the dependent parameters, thermal and exergy efficiency, was found to be ± 2.2% and ± 1.5% respectively.

$$\frac{\delta\eta_{th}}{\eta_{th}} = \sqrt{\left(\frac{\delta m}{m}\right)^2 + \left(\frac{\delta \Delta T_{in}}{\Delta T_{in}}\right)^2 + \left(\frac{\delta \Delta T_{out}}{\Delta T_{out}}\right)^2 + \left(\frac{\delta I}{\Delta I}\right)^2} \quad (18)$$

$$\frac{\delta\eta_{ex}}{\eta_{ex}} = \sqrt{\left(\frac{\delta m}{m}\right)^2 + \left(\frac{\delta \Delta T_{in}}{\Delta T_{in}}\right)^2 + \left(\frac{\delta \Delta T_{out}}{\Delta T_{out}}\right)^2 + \left(\frac{\delta T_{amb}}{T_{amb}}\right)^2 + \left(\frac{\delta I}{I}\right)^2} \quad (19)$$

6.4. Energy and Exergy analysis

From Fig. 17, it is observed that the maximum optical efficiency of 75% is obtained when direct solar radiation is received at zero incidence angles. The various results of experimentation performed on nanofluid applied PTDASC at different flow rates are shown in Figs. 18, 19 and 20. The Figs. 18, 19 and 20 (c) illustrates the solar irradiation data received on each test day. The scattering observed in the energy and exergy efficiency curves in Figs. 18 and 19 (b) can be attributed to the thermal inertia during volumetric absorption. The variation in the solar irradiation received by the parabolic trough collector will affect the outlet temperature of the nanofluid which in turn produces the fluctuation in efficiency curves [44, 45]. The efficiency curve at the highest flow rate, Fig. 18 (b), shows that almost 90% of the data points corresponding to the instantaneous thermal efficiency of the solar collector was falling within a range of 40% to 60%. In the case of lower flow rates, the thermal efficiencies were varying in a smaller range which showed consistent results. The variation of instantaneous thermal and exergy efficiency with time for base fluid with flow rates of 0.016, 0.019 and 0.022 kgs^{-1} is shown in Fig. 21 (a), (b) and (c) respectively. The variation in thermal and exergy efficiency of the hybrid nanofluid applied DASC with temperature difference across the receiver length was plotted for three different mass flow rates. The graphs Figs. 18, 19 and 20 (b), throws light on the dependence of efficiencies on the temperature difference attained. As observed in Fig. 18 (b), the thermal efficiency was increasing linearly with the rise in temperature difference across the tube length. Even though the exergy efficiency exhibited almost a similar trend as that of thermal efficiency, the highest exergy and thermal efficiencies were not occurring for the same nanofluid temperature gain. The highest exergy efficiency corresponded to the achievement of 8°C difference in nanofluid temperature across the system, while the peak thermal efficiency was pertaining to a rise of 12.6 °C. Also, in the case of

Fig. 19 and 20 (b), the trendlines of the efficiencies were almost parallel. The temperature difference between the inlet and outlet of the receiver was observed to increase with a decrease in the flow rate of the working fluids. The outlet temperature of the nanofluid increased by 3˚C when the flow rate was decreased from 0.022 kgs^{-1} to 0.016 kgs^{-1}.

From the experimental data obtained, the variation of thermal and exergy efficiency with solar irradiation is plotted as shown in Fig. 22. Thermal and exergy efficiency was observed to increase with the increase in solar irradiance. A decrease in the exergy efficiency was noticed with an increase in solar irradiance above 800 Wm^{-2} while thermal efficiency was observed to increase. It could be concluded that higher solar flux can produce more heat loss from the system. The effect of heat loss on the exergy efficiency is higher compared to that of energy efficiency. Incident solar irradiation was found to be having a predominant effect on the thermal efficiency enhancement when compared with exergy efficiency. The variation of thermal and exergy efficiency of the collector with flow rates is shown in Fig. 23. It is observed that the maximum efficiency of the collector was pertaining to the maximum flow rate. The highest thermal efficiency and exergy efficiency observed was 63.5% and 5.6% respectively at a flow rate of 0.022 kgs^{-1}. As the flow rate increased from 0.016 kgs^{-1} to 0.019 $kgs^{-1}$and 0.022 kgs^{-1}, the thermal efficiency increased by 3.1% and 5.3% respectively, and the corresponding increase in exergy efficiency was 11.8% and 17.68%, respectively. The substantial rise in the exergy efficiency when compared to thermal efficiency shows that the former is more dependent on solar irradiation while the latter is easily controlled by flow rate. Hence optimization of the working parameters is required for the collector's efficient performance. Exergy efficiency is dependent on the fluid inlet and outlet temperatures, incident solar radiation and the ambient temperature. As the flow rate increases the loss of heat from the collector is reduced as the time spent by nanofluid in the receiver is less. Hence an increase in thermal and exergy efficiency will be observed. Also, the maximum nanofluid outlet temperature increased with a decrease in flow rate. As the flow rate decreased, more energy conversion took place due to absorption and scattering.

If the ambient temperature of the surrounding is high, then the exergy efficiency will be high compared to the same conditions at lower ambient conditions. So, as the exergy varies due to more factors compared to thermal efficiency, a linear relationship between these efficiencies could not

546 be stated from the results obtained. Also, the exergy efficiency is only important at inferring the
547 necessary heat loss reducing methods and not a factor at evaluating the applicability of the system.

548

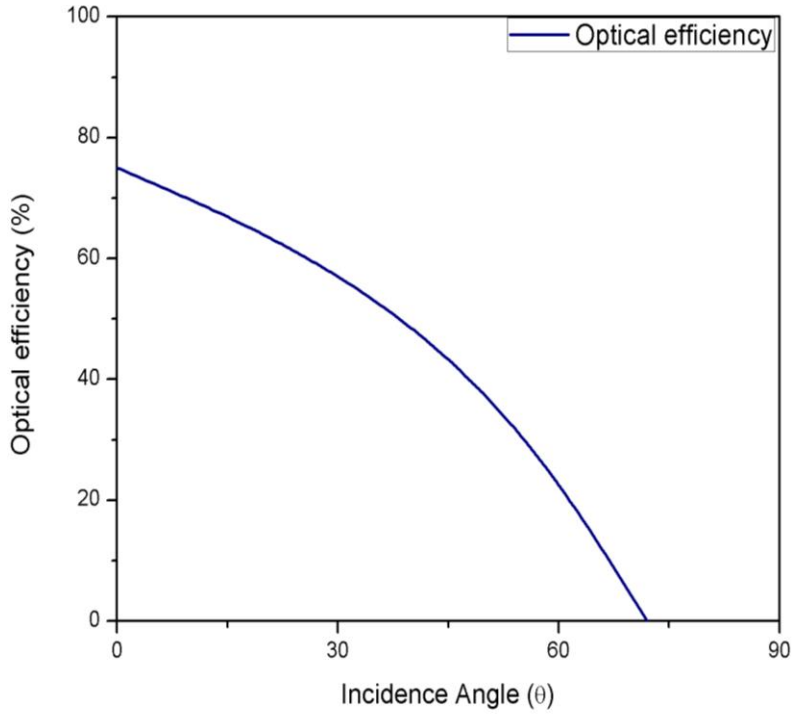

549

550 **Fig. 17.** Variation of optical efficiency with incidence angle

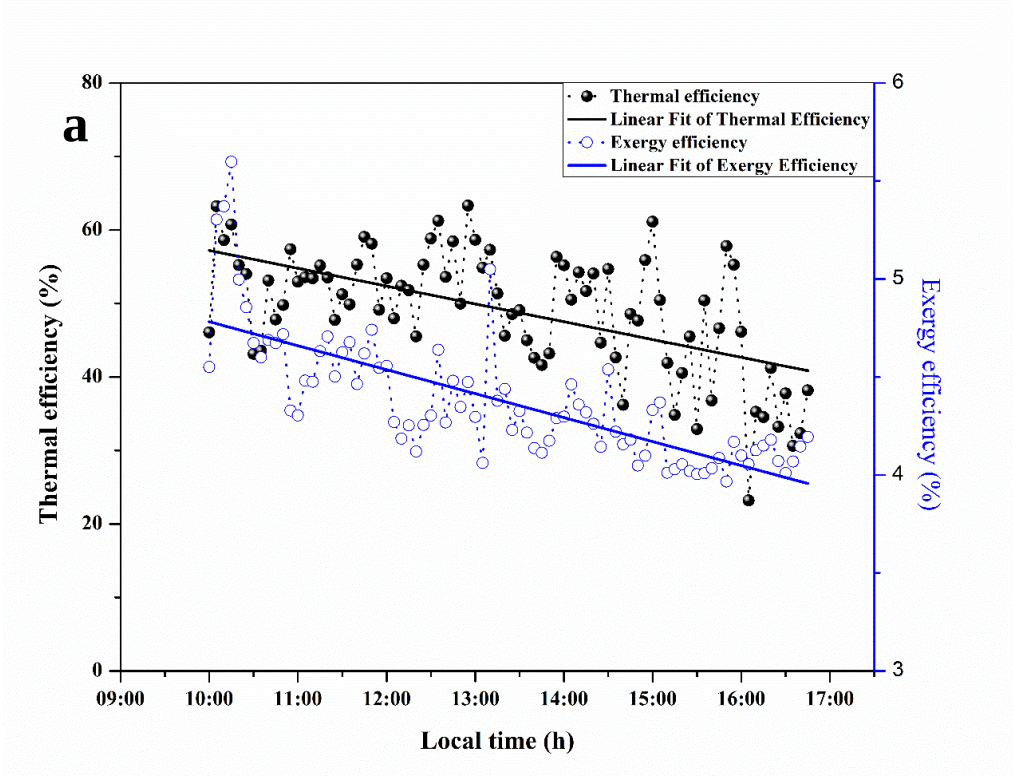
a
Thermal efficiency
Linear Fit of Thermal Efficiency
Exergy efficiency
Linear Fit of Exergy Efficiency
Thermal efficiency (%)
Exergy efficiency (%)
Local time (h)
09:00
10:00
11:00
12:00
13:00
14:00
15:00
16:00
17:00

551

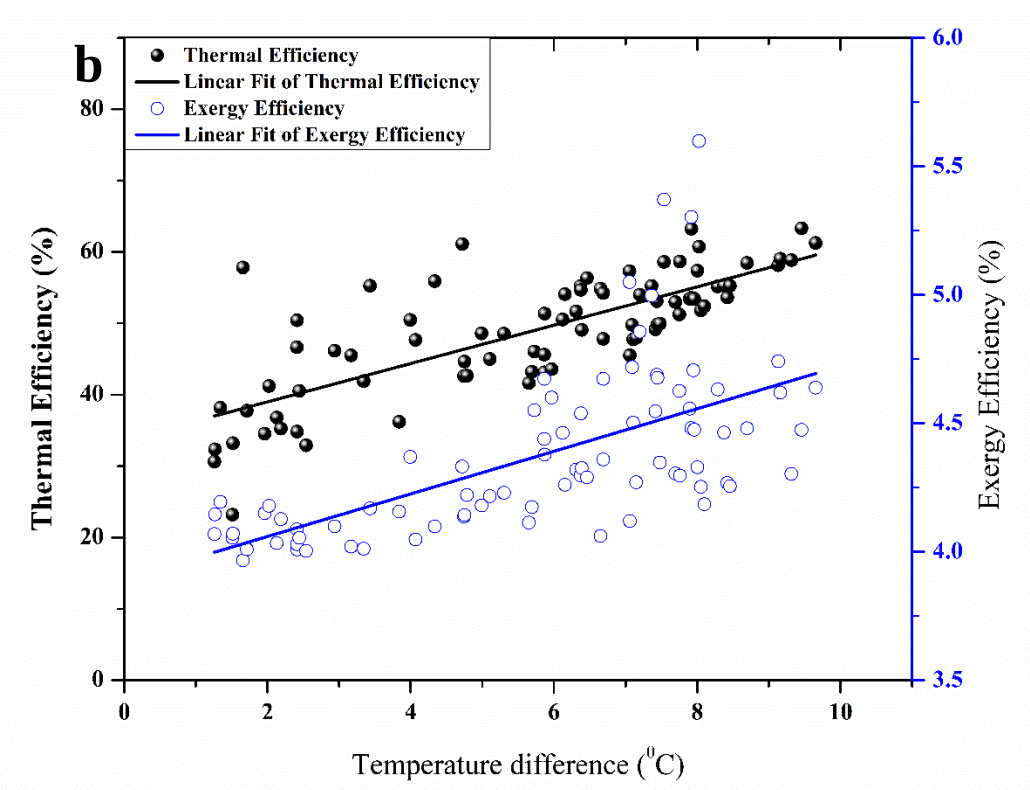
b
Thermal Efficiency
Linear Fit of Thermal Efficiency
Exergy Efficiency
Linear Fit of Exergy Efficiency
Thermal Efficiency (%)
Exergy Efficiency (%)
Temperature difference (°C)

552

553

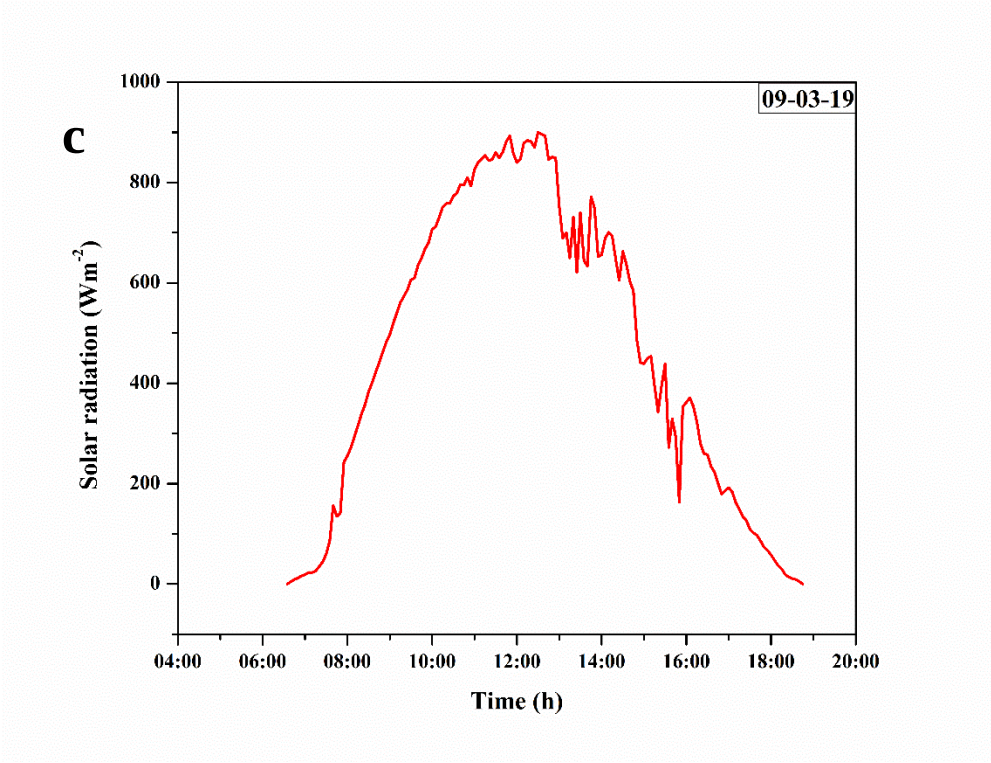

554

555 **Fig. 18.** (a) Thermal and exergy efficiency of PTDASC at 0.022 kgs^{-1}, (b) Variation of thermal
556 and exergy efficiency with temperature difference (c) Solar radiation data for 09-03-19

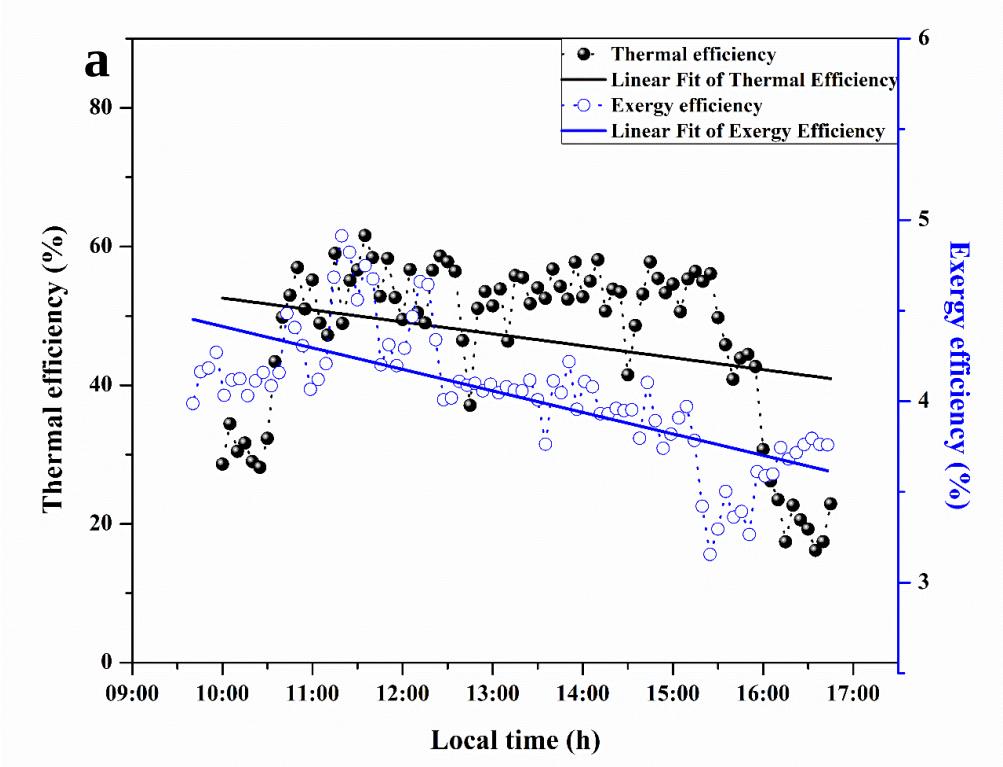

557

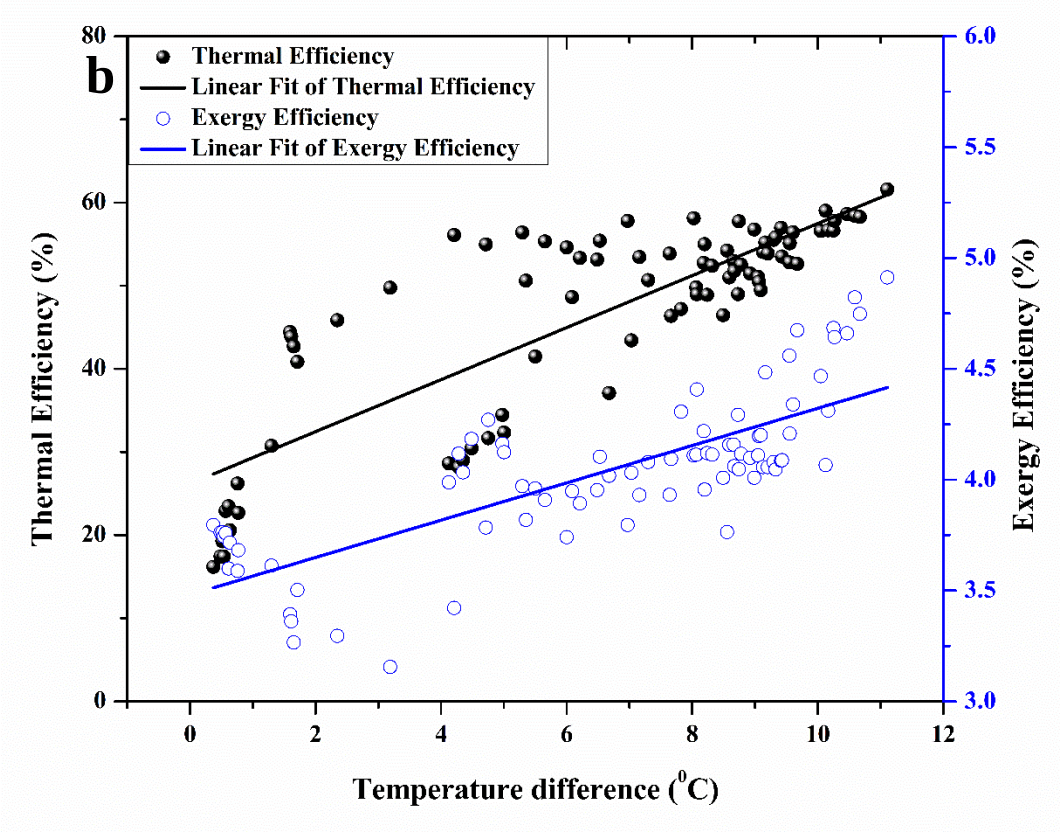

558

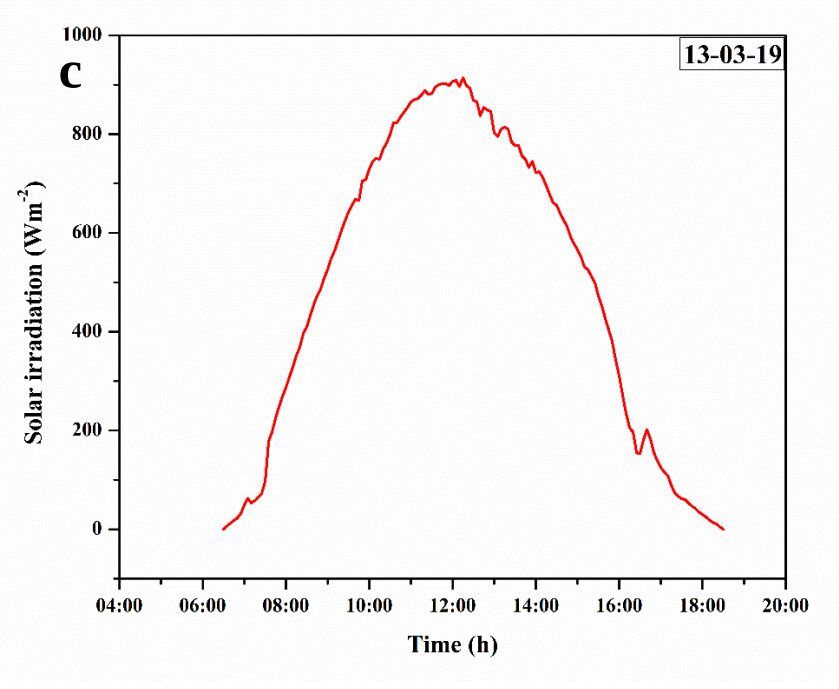

559

560 **Fig. 19.** (a) Thermal and exergy efficiency of PTDASC at 0.019 kgs^{-1}, (b) Variation of thermal
561 and exergy efficiency with temperature difference (c) Solar radiation data for 13-03-19

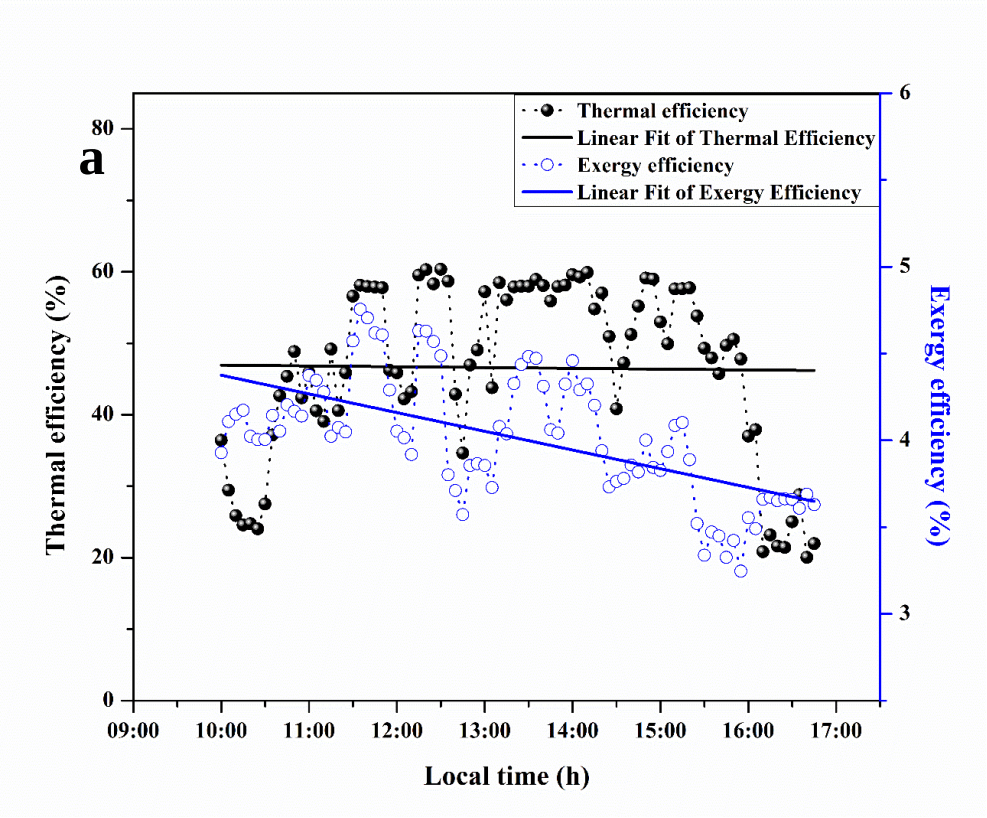
a
Thermal efficiency
Linear Fit of Thermal Efficiency
Exergy efficiency
Linear Fit of Exergy Efficiency
Thermal efficiency (%)
Exergy efficiency (%)
Local time (h)
0
20
40
60
80
3
4
5
6
09:00
10:00
11:00
12:00
13:00
14:00
15:00
16:00
17:00

562

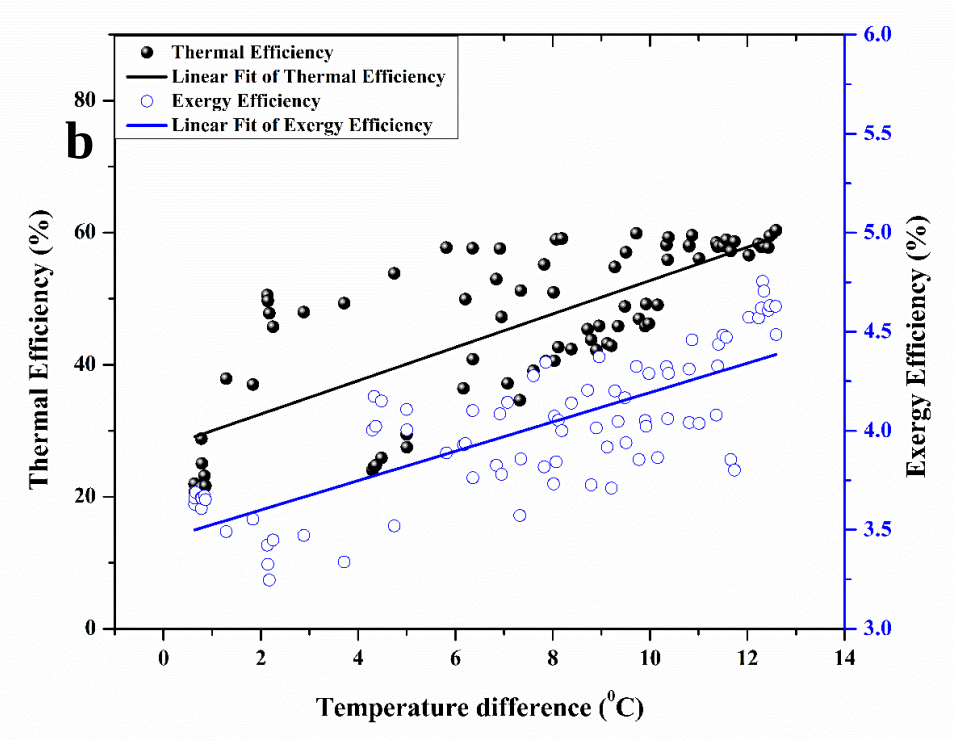
b
Thermal Efficiency
Linear Fit of Thermal Efficiency
Exergy Efficiency
Linear Fit of Exergy Efficiency
Thermal Efficiency (%)
Exergy Efficiency (%)
Temperature difference (°C)
0
20
40
60
80
3.0
3.5
4.0
4.5
5.0
5.5
6.0
0
2
4
6
8
10
12
14

563

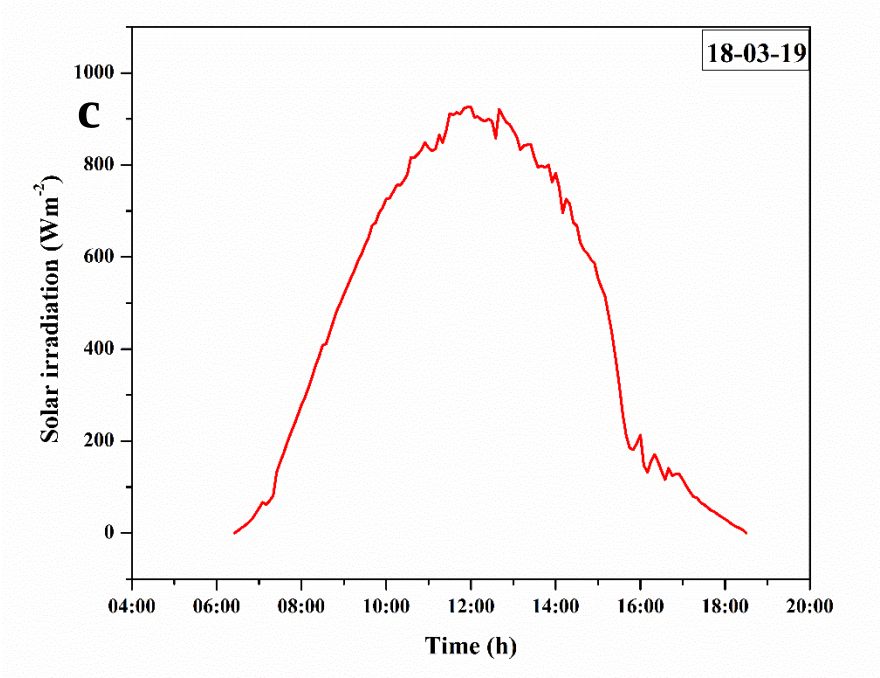

564

565 **Fig. 20.** (a) Thermal and exergy efficiency of PTDASCC at 0.016 kgs^{-1}, (b) Variation of thermal
566 and exergy efficiency with temperature difference (c) Solar radiation data for 18-03-19

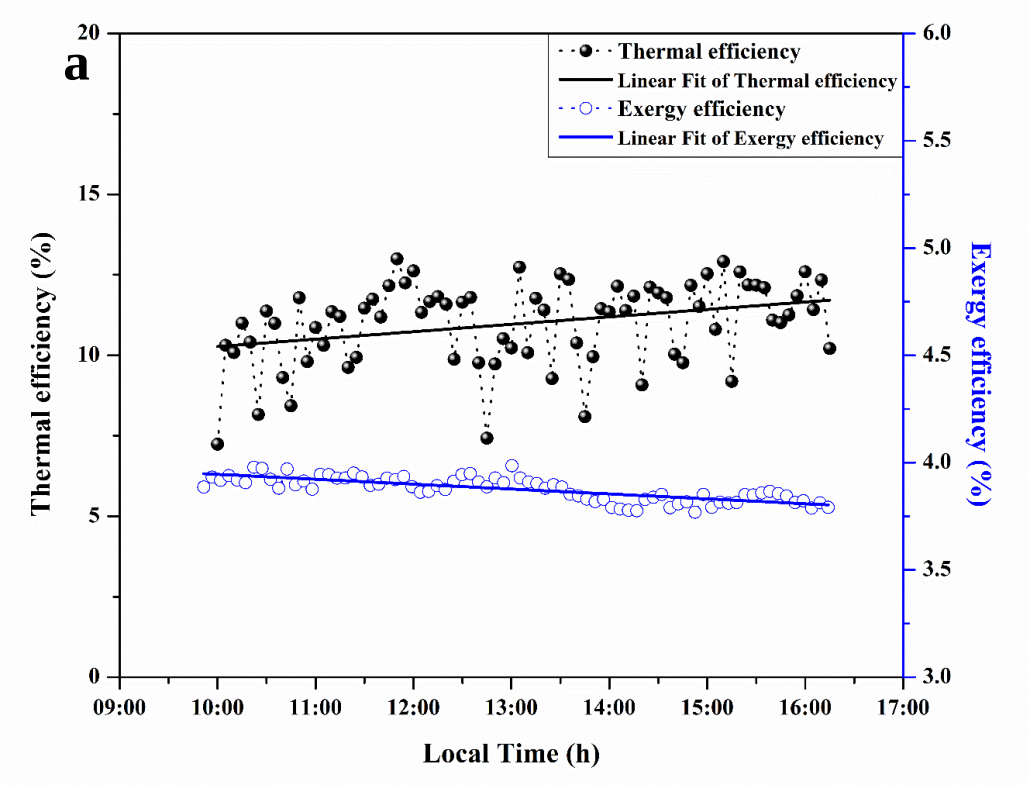

567

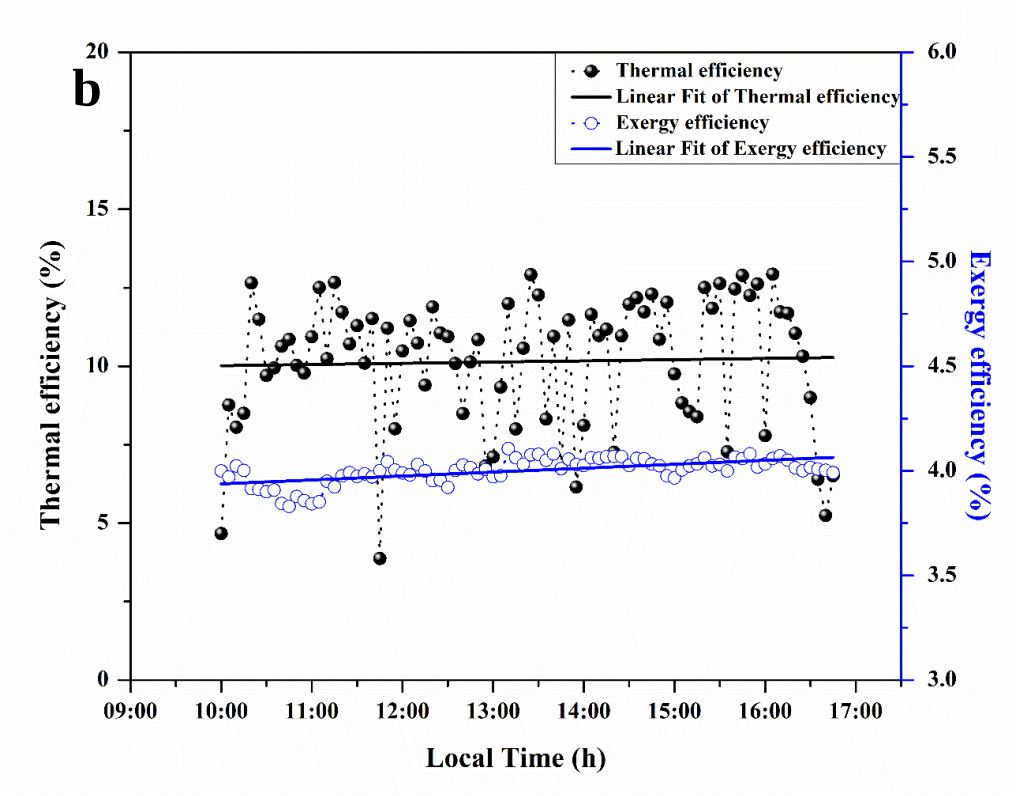

568

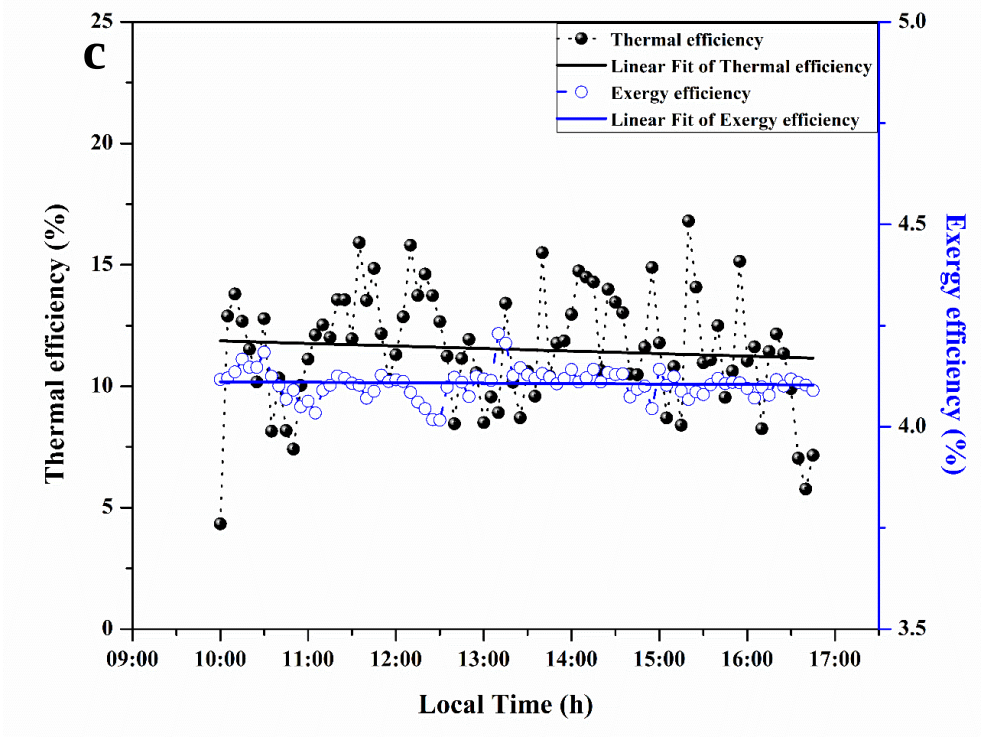

569

570 **Fig. 21.** Thermal and exergy efficiency of PTC run with base fluid at (a) 0.016 kgs^{-1}, (b) 0.019

571 kgs^{-1} and (c) 0.022 kgs^{-1}

572

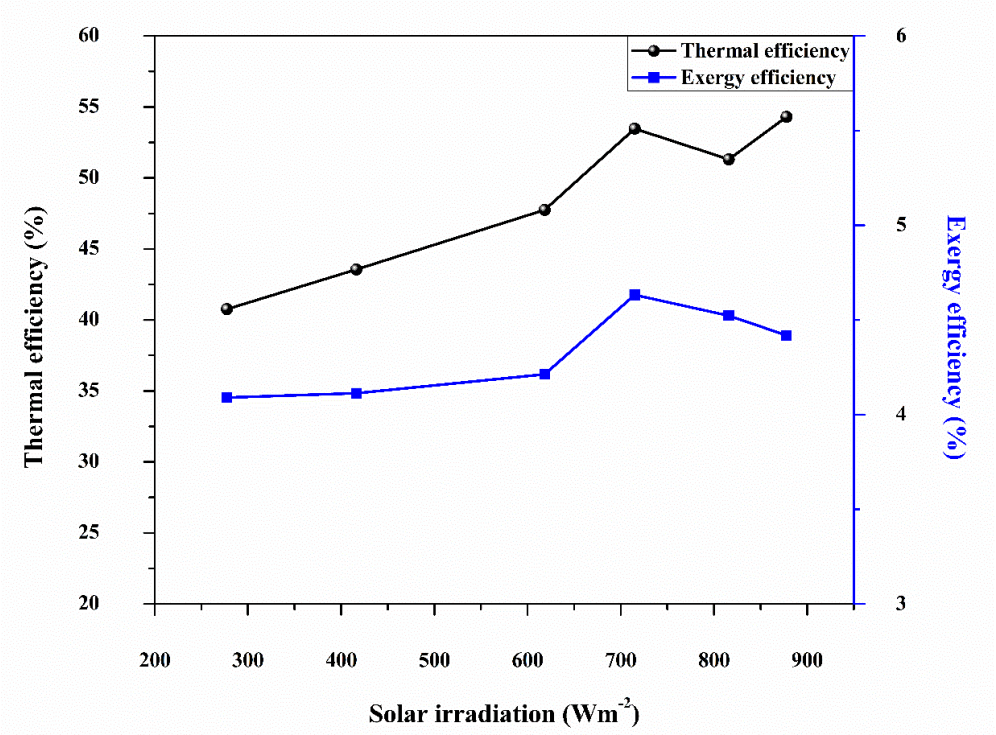

573

574 **Fig. 22.** Variation of thermal efficiency and exergy efficiency with solar irradiation

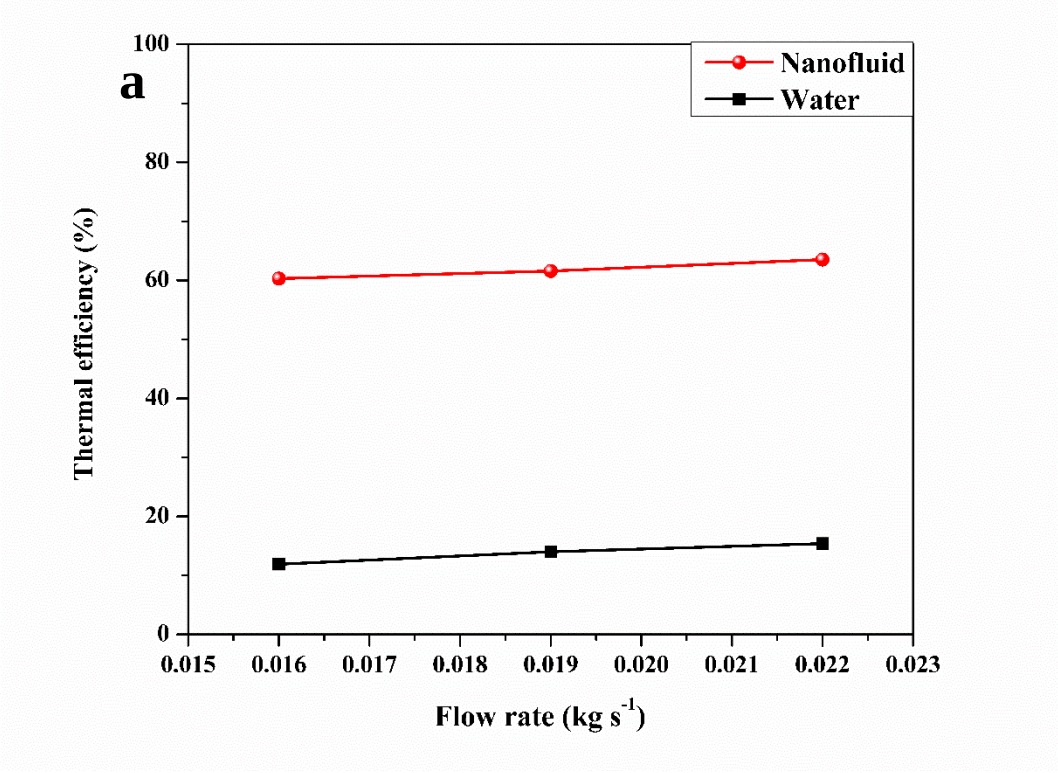

575

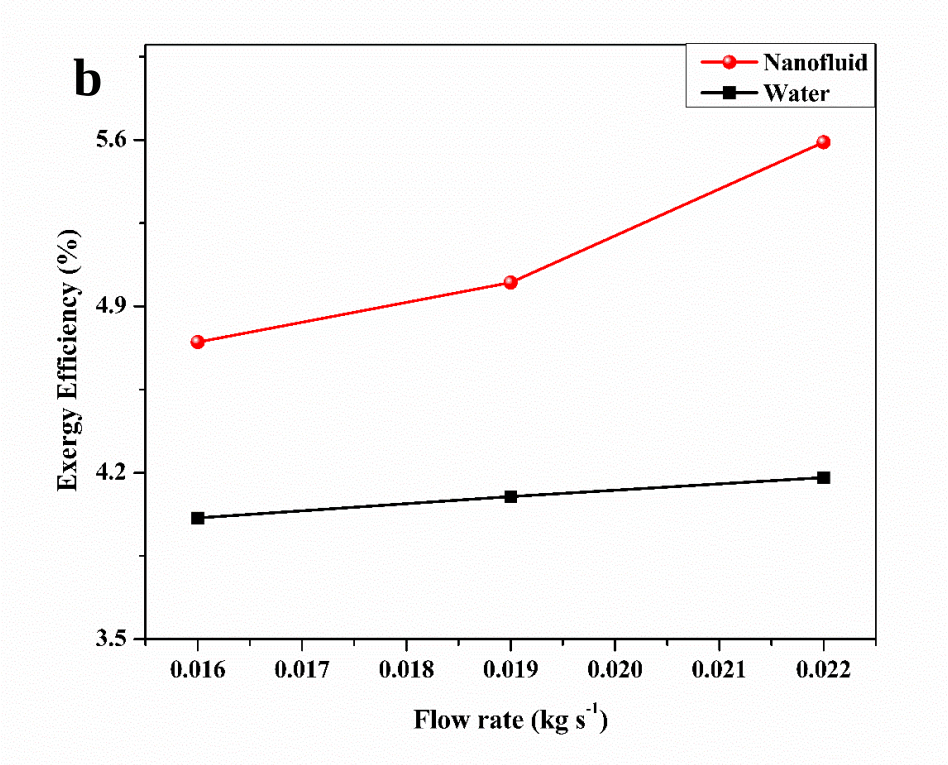

Fig. 23. Variation of (a) thermal efficiency and (b) exergy efficiency with the flow rate

A trendline of thermal and exergy efficiency of the parabolic trough collector at three different flow rates was generated based on the statistical linear curve fitting technique. The coefficients and trendline equations of the corresponding curve are given in Table 6. The slope of the line is represented by 'b', while 'a' represents the intercept of the fitted line. R^2 represents the adjacent R-squared value for each flow rate.

Table 6: Coefficients of efficiency curve at different flow rates

Working Fluid	**Flow rate**								
	0.022 kgs^{-1}			0.019 kgs^{-1}			0.016 kgs^{-1}		
Nanofluid	**R^2**	**a**	**b**	**R^2**	**a**	**b**	**R^2**	**a**	**b**
Thermal efficiency	0.587	33.62	0.30	0.675	26.18	3.12	0.573	27.4	2.52
	$\eta_{th} = a + b\Delta T$			$\eta_{th} = a + b\Delta T$			$\eta_{th} = a + b\Delta T$		
Exergy efficiency	0.377	3.89	0.08	0.586	3.48	0.084	0.588	3.45	0.07
	$\eta_{ex} = a + b\Delta T$			$\eta_{ex} = a + b\Delta T$			$\eta_{ex} = a + b\Delta T$		

Nanofluid applied solar collectors face the problem of the settling of nanomaterial in the receiver tube. The sedimentation method, as depicted in section 5.4, validates that only a meagre deposition of nanoparticles was observed. In the present system, the nanomaterial which has sedimented on the tube surface after continuous operation for 8 hours was less. An increase in pressure drop due to higher viscosity is a setback associated with the usage of nanofluid [20]. However, the increase in pumping power due to pressure drop was found to be insignificant in the present study. Another issue is the degradation of the optical absorptivity property of nanofluid. Analysis of the retainability of nanofluid's optical absorption was performed, as given in section 6.5.

6.5. Analysis of the degradation rate of solar weighted absorption fraction

Spectral absorption analysis was employed to analyze the deterioration of stability of optimized nanofluid after being deployed in the solar collector system. Transmittance spectra of nanofluid, before and after running through the hydraulic cycle, is given in Fig. 29. Solar weighted absorption fraction calculated for nanofluid, before and after circulation in the parabolic trough system was observed to be 89% and 88% respectively. A marginal decrease in nanofluid's solar weighted absorption fraction of 1.12% was observed at the end of experimentation. It is concluded that the optimized concentration is not undergoing any degradation in performance due to stability or other issues even after circulating through the hydraulic loop.

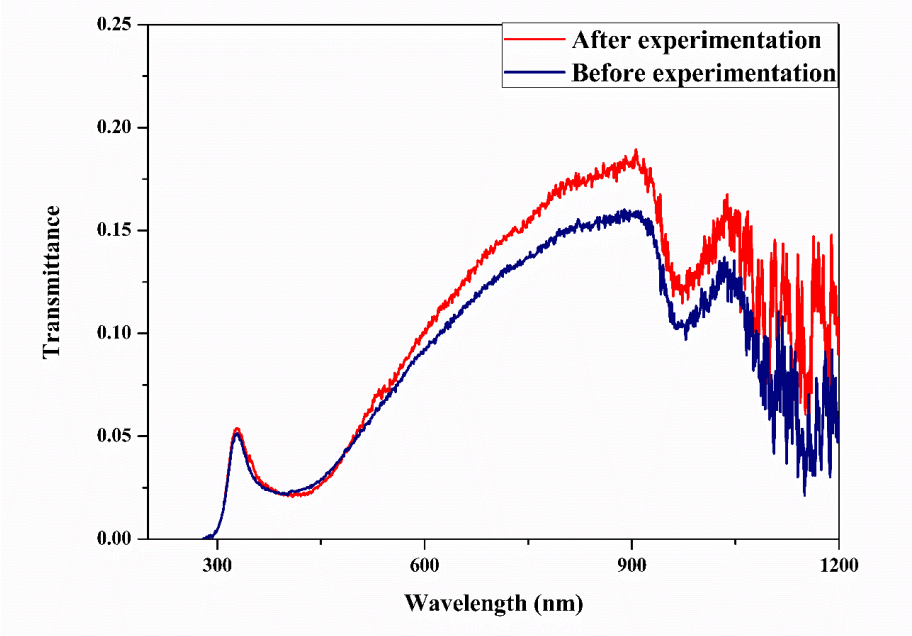

Fig. 24. Spectroscopic analysis of optimized nanofluid before and after experimentation in the solar collector

7. Conclusions

The synthesis and characterization of visible and NIR spectrum absorption concentrated ATO/Ag hybrid nanoparticles have been performed. TEM analysis shows the morphology of silver nanoparticles attached to the surface of ATO nanoparticles. XRD analysis was performed and phase characterization of the hybrid nanoparticle is done. SEM-EDAX and XRD confirm the presence of as stated components in the hybrid nanoparticle. RSM using Central Composite Design produced a minimum of 13 sets of experimental runs. Model prediction of solar weighted absorption fraction is in agreement with the actual data obtained. The relative error between the actual and the predicted value being very less validates the model predictability. Solar weighted absorptivity is observed to be linearly dependent on nanoparticle concentration. The maximum solar weighted absorptivity of 98.90% is obtained at 0.2% ATO/Ag and 0.15% SDS. The optimization of concentrations of nanoparticle and surfactant was performed based on the calculated solar weighted absorptivity of each run. Parametric investigation of the effect of penetration depth on solar weighted absorption fraction and mass fraction on the extinction coefficient was performed. Solar weighted absorption fraction was found to increase exponentially with penetration depth. The extinction coefficient increased linearly with the mass fraction. Investigations on direct absorption parabolic trough solar collectors yielded an optical efficiency of 75% while using ATO/Ag nanofluid. Energy and exergy efficiency were found to be a linear function of the mass flow rate. The highest thermal efficiency obtained for ATO/Ag hybrid nanofluid in PTDASC was 63.5 %. The exergy efficiency of 5.6 % indicates the need to reduce heat loss. The temperature difference across the receiver length decreased with an increase in flow rate. 25% rise in temperature difference was reported on changing flow rate from $0.022\ kgs^{-1}$ to $0.016\ kgs^{-1}$. It could be concluded from the obtained results, that as the flow rate increases, heat loss is reduced, thereby increasing the energy and exergy efficiency.

References

[1] R.A. Taylor, P.E. Phelan, T.P. Otanicar, C.A. Walker, M. Nguyen, S. Trimble, R. Prasher, Applicability of nanofluids in high flux solar collectors, J. Renew. Sustain. Energy 3 (2) (2011) 023104. https://doi.org/10.1063/1.3571565.

[2] J.E. Minardi, H.N. Chuang, Performance of a black liquid flat-plate solar collector, Sol.

Energy 17 (1975) 179-183. https://doi.org/10.1016/0038-092X(75)90057-2.

[3] H. Tyagi, P.E. Phelan, R. Prasher, Predicted efficiency of a low-temperature nanofluid-based direct absorption solar collector, J. Sol. Energy Eng. 131 (2009) 041004. https://doi.org/10.1115/1.3197562.

[4] T.P. Otanicar, P.E. Phelan, J. S. Golden, Optical properties of liquids for direct absorption solar thermal energy systems, Sol. Energy 83 (2009) 969–977. https://doi.org/10.1016/j.solener.2008.12.009.

[5] M. Chen, Y. He, J. Huang, J. Zhu, Investigation into Au nanofluids for solar photothermal conversion, Int. J. Heat Mass Transf. 108 (2017) 1894–1900. https://doi.org/10.1016/j.ijheatmasstransfer.2017.01.005.

[6] C.L.L. Beicker, M. Amjad, Enio P. Bandarra Filho, Dongsheng Wen, Experimental study of photothermal conversion using gold/water and MWCNT/water nanofluids, Sol. Energy Mater. Sol. Cells 188 (2018) 51–65. https://doi.org/10.1016/j.solmat.2018.08.013.

[7] M. Amjad, H. Jin, X. Du, D. Wen, Experimental photothermal performance of nanofluids under concentrated solar flux, Sol. Energy Mater. Sol. Cells 182 (2018) 255–262. https://doi.org/10.1016/j.solmat.2018.03.044.

[8] A.S. Abdelrazika, F.A. Al-Sulaimana, R. Saidur, Optical behavior of a water/silver nanofluid and their influence on the performance of a photovoltaic-thermal collector, Sol. Energy Mater. Sol. Cells 201 (2019) 110054. https://doi.org/10.1016/j.solmat.2019.110054

[9] M. Valizade, M.M. Heyhat, M. Maerefat, Experimental comparison of optical properties of nanofluid and metal foam for using in direct absorption solar collectors, Sol. Energy Mater. Sol. Cells 195 (2019) 71–80. https://doi.org/10.1016/j.solmat.2019.01.050.

[10] N. Chen, H. Ma, Y. Li, J. Cheng, C. Zhang, D. Wu, H. Zhu, Complementary optical absorption and enhanced solar thermal conversion of CuO-ATO nanofluids, Sol. Energy Mater. Sol. Cells 162 (2017) 83–92. https://doi.org/10.1016/j.solmat.2016.12.049.

[11] F. Yu, Y. Chen, X. Liang, J. Xu, C. Lee, Q. Liang, P. Tao, T. Deng, Dispersion stability of thermal nanofluids, Prog. Nat. Sci. Mater. Int. 27 (2017) 531-542. https://doi.org/10.1016/j.pnsc.2017.08.010.

[12] X. Yu, Y. Xuan, Investigation on thermo-optical properties of CuO/Ag plasmonic nanofluids, Sol. Energy 160 (2018) 200–207.

https://doi.org/10.1016/j.solener.2017.12.007.

[13] Q. Jiang, W. Zeng, C. Zhang, Z. Meng, J. Wu, Q. Zhu, D. Wu, H. Zhu, Broadband absorption and enhanced photothermal conversion property of octopod-like Ag@Ag2S core@shell structures with gradually varying shell thickness, Nature 7 (2017) 17782. https://doi.org/10.1038/s41598-017-18220-1.

[14] J. Zeng, Y. Xuan, H. Duan, Tin-silica-silver composite nanoparticles for medium-to-high temperature volumetric absorption solar collectors, Sol. Energy Mater. Sol. Cells 157 (2016) 930–936. https://doi.org/10.1016/j.solmat.2016.08.012.

[15] J. Zeng, Y. Xuan, Enhanced solar thermal conversion and thermal conduction of MWCNT-SiO_2/Ag binary nanofluids, Appl. Energy 212 (2018) 809–819. https://doi.org/10.1016/j.apenergy.2017.12.083.

[16] J. Zeng, Y. Xuan, Tunable Full-Spectrum Photo-thermal Conversion Features of Magnetic-Plasmonic Fe3O4/TiN Nanofluid, NANO ENERGY 2855 (18) 30522-6. https://doi.org/10.1016/j.nanoen.2018.07.034.

[17] A. Joseph, S. Mohan, C.S. Sujith Kumar, A. Mathew, S. Thomas, B.R. Vishnu, S.P. Sivapirakasam, An experimental investigation on pool boiling heat transfer enhancement using sol-gel derived nano-CuO porous coating, Exp. Therm. Fluid Sci. 103 (2019) 37–50. https://doi.org/10.1016/j.expthermflusci.2018.12.033.

[18] M. Hemmat Esfe, M. Firouzi, H. Rostamian, M. Afrand, Prediction and optimization of thermophysical properties of stabilized Al2O3/antifreeze nanofluids using response surface methodology, J. Mol. Liq. 261 (2018) 14–20 https://doi.org/10.1016/j.molliq.2018.03.063.

[19] T.P Otanicar, Direct absorption solar thermal collectors utilizing liquid-nanoparticle suspensions. Doctor of Philosophy, Arizona State University; 2009.

[20] A.A. Minea, W. M. El-Maghlany, Influence of hybrid nanofluids on the performance of parabolic trough collectors in solar thermal systems: Recent findings and numerical comparison, Renew. Energy 1481 (17) 31297-1. https://doi.org/10.1016/j.renene.2017.12.093.

[21] E. Bellos, C. Tzivanidis, Thermal analysis of parabolic trough collector operating with mono and hybrid nanofluids, Sustain. Energy Technol. Assess. https://doi.org/10.1016/j.seta.2017.10.005.

[22] S. Delfani, M. Karami, M.A. Akhavan-Bahabadi, Performance characteristics of a residential-type direct absorption solar collector using MWCNT nanofluid, Renew. Energy 87 (2016) 754–764. https://doi.org/10.1016/j.renene.2015.11.004.

[23] M. Vakili, S. M. Hosseinalipour, S. Delfani, S. Khosrojerdi, and M. Karami, Experimental investigation of graphene nanoplatelets nanofluid-based volumetric solar collector for domestic hot water systems, Sol. Energy 131 (2016) 119–130. https://doi.org/10.1016/j.solener.2016.02.034.

[24] A. Menbari, A.A. Alemrajabi, A. Rezaei, Heat transfer analysis and the effect of CuO/Water nanofluid on direct absorption concentrating solar collector, Appl. Therm. Eng. 104 (2016) 176–183. https://doi.org/10.1016/j.applthermaleng.2016.05.064.

[25] A. Menbari, A.A. Alemrajabi, A. Rezaei, Experimental investigation of thermal performance for direct absorption solar parabolic trough collector (DASPTC) based on binary nanofluids, Exp. Therm. Fluid Sci. 80 (2017) 218-227. https://doi.org/10.1016/j.expthermflusci.2016.08.023.

[26] S.A. Kalogirou, S. Karellas, V. Badescu, K. Braimakis, Exergy analysis on solar thermal systems: A better understanding of their sustainability. Renew Energy 85 (2016) 1328–33. https://doi.org/10.1016/j.renene.2015.05.037.

[27] T.B. Gorji, A.A. Ranjbar, Thermal and exergy optimization of a nanofluid-based direct absorption solar collector, Renew. Energy 106 (2017) 274-287. https://doi.org/10.1016/j.renene.2017.01.031.

[28] M. Karami, Experimental investigation of first and second laws in a direct absorption solar collector using hybrid Fe3O4/SiO2 nanofluid, J Therm Anal Calorim 136 (2019) 661-667. https://doi.org/10.1007/s10973-018-7624-x.

[29] Z. Zhang, Y. Ma, X. Bu, Q. Wu, Z. Hang, Z. Dong, X. Wu, Facile one-step synthesis of TiO2/Ag/SnO2 ternary heterostructures with enhanced visible light photocatalytic activity, Nature 8 (2018)10532. https://doi.org/10.1038/s41598-018-28832-w.

[30] M. Kosmulski, Isoelectric points and points of zero charge of metal (hydr)oxides: 50 years after Parks' review, Adv. Colloid Interface Sci. 238 (2016) 1–61. https://doi.org/10.1016/j.cis.2016.10.005.

[31] A. R. Mallah, S. N. Kazi, M. N. M. Zubir, A. Badarudin, Blended morphologies of plasmonic nanofluids for direct absorption applications, Appl. Energy 229 (2018) 505–521. https://doi.org/10.1016/j.apenergy.2018.07.113.

[32] W.D. Drotning, Optical properties of solar-absorbing oxide particles suspend in a molten salt heat transfer fluid, Sol. Energy 20 (1978) 313–319. https://doi.org/10.1016/0038-092X(78)90123-8.

[33] ASTM G173-03, Standard Tables for Reference Solar Spectral Irradiances: Direct Normal and Hemispherical on 37 Tilted Surface, ASTM International, West Conshohocken, 2012.

[34] P.D. Nasab, A.R. Kelishami, J. Safdari, H. Abolghasemi, Application of emulsion nanofluids membrane for the extraction of gadolinium using response surface methodology, J. Mol. Liq. 244 (2017) 368-373. http://dx.doi.org/10.1016/j.molliq.2017.08.127.

[35] X. Lei, J. Shuang, P. Yang, Y. Liu, Parametric study and optimization of dimpled tubes based on Response Surface Methodology and desirability approach, Int. J. Heat Mass Transf. 142 (2019) 118453. https://doi.org/10.1016/j.ijheatmasstransfer.2019.118453.

[36] M.U. Sajid, H. M. Ali, Thermal conductivity of hybrid nanofluids: A critical review, Int. J. Heat Mass Transf. 126 (2018) 211–234. https://doi.org/10.1016/j.ijheatmasstransfer.2018.05.021.

[37] M.S. Bretado de los Rios, C.I. Rivera-Solorio, A.J. García-Cu_ellar, Thermal performance of a parabolic trough linear collector using Al2O3/H2O nanofluids, Renew. Energy 122 (2018) 665-673. https://doi.org/10.1016/j.renene.2018.01.094

[38] A. Kasaeian, S. Daviran, R. D. Azarian, A. Rashidi, Performance evaluation and nanofluid using capability study of a solar parabolic trough collector, J. Clean. Prod. 89 (2015) 368–375. https://doi.org/10.1016/j.enconman.2014.09.056.

[39] ASHRAE Standard 93. Method of testing to determine the thermal performance of solar collectors. Atlanta (GA): American Society of Heating, Refrigerating and Air-Conditioning Engineers; 2010.

[40] R. Petela, Exergy of undiluted thermal radiation, Sol. Energy 74 (2003) 469–488. https://doi.org/10.1016/S0038-092X(03)00226-3.

[41] I. Ceylan, A. Ergun, Thermodynamic analysis of a new design of temperature controlled parabolic trough collector, Energy Convers. Manag. 74 (2013) 505–510. https://doi.org/10.1016/j.enconman.2013.07.020.

[42] Q. Wang, M. Hu, H. Yang, J. Cao, J. Li, Y. Su, G. Pei, Energetic and exergetic analyses on structural optimized parabolic trough solar receivers in a concentrated solar thermal collector system, Energy, 171 (2019) 611-623. https://doi.org/10.1016/j.energy.2018.12.211.

[43] R. J. Moffat, Describing the uncertainties in the experimental results, Exp. Therm. Fluid Sci. 1 (1985) 3-17. https://doi.org/10.1016/0894-1777(88)90043-X.

[44] M. Chafie, M.F.B. Aissa, A. Guizani, Energetic end exergetic performance of a parabolic trough collector receiver: An experimental study, J. Clean. Prod. 171 (2018) 285-296.

[45] M. Fana, H. Lianga, S. Youa, H. Zhanga, B.Yinb, X. Wu, Applicability analysis of the solar heating system with parabolic trough solar collectors in different regions of China, Appl. Energy 221 (2018) 100–111. https://doi.org/10.1016/j.apenergy.2018.03.137.

629